Remote sensing-based ecosystem–atmosphere simulation scheme (EASS)—Model formulation and test with multiple-year data

Baozhang Chen*, Jing M. Chen, Weimin Ju

Department of Geography and Program in Planning, University of Toronto, Ont., Canada

ABSTRACT

A new remote-sensing-based land surface model, named ecosystem–atmosphere simulation scheme (EASS), is introduced in this paper. The principle motivation for formulating EASS is to provide realistic partition of energy fluxes at regional scales as well as consistent estimates of carbon assimilation rates. EASS has the following characteristics: (i) satellite data are used to describe the spatial and temporal information on vegetation, and in particular, we use a foliage clumping index (Ω) in addition to leaf area index to characterize the effects of three-dimensional canopy structure on radiation, energy and carbon fluxes; (ii) energy and water exchanges and carbon assimilation in the soil–vegetation–atmosphere system are fully coupled and are simulated simultaneously; (iii) the energy and carbon assimilation fluxes are calculated with stratification of sunlit and shaded leaves to avoid shortcomings of the "big-leaf" assumption. Model experiments shows that the simulation realism and accuracy by the new strategy are enhanced about 9–14% compared with the "big-leaf model". Moreover, Ω is useful for accurate separation of sunlit and shaded leaves in the canopy. The accuracy in simulation of energy and carbon fluxes increase about 5–8% by considering the effects of Ω on the radiation interception and the separation of sunlit and shaded leaves; (iv) snow and soil simulations are emphasized by including a flexible and multiple layer scheme. EASS has been tested and validated against multiple-year observed data at several sites. EASS is proved to be overall successful in capturing variations in energy fluxes, canopy and soil temperatures, and soil moisture over diurnal, synoptic, seasonal and inter-annual temporal scales.

1. Introduction

The land surface of the Earth represents significant sources, sinks, and reservoirs of heat and moisture to the atmosphere. Energy fluxes and water cycles at soil–atmosphere and plant–atmosphere interfaces are therefore important land surface processes. It is well known that realistic simulations of land surface processes is of critical importance, not only for the surface microclimate, but also for the large-scale physics of the atmosphere (Pleim and Xiu, 2003). The development of land surface models (LSMs) can be flagged by the 'first-generation' (e.g., Manabe, 1969; Carson, 1982) and the 'second-generation' (e.g., BATS, Dickinson et al., 1986, 1992; SiB, Sellers et al., 1986; BEST, Pitman et al., 1991; CLASS, Verseghy, 1991; Verseghy et al., 1993). Marked improvements of the second generation from the first generation are the

Nomenclature

a_v a constant used in Eq. (26), it depends on vegetation type with a varying range of 0.15–0.25

A_l leaf net photosynthesis assimilation ($\mu mol\,m^{-2}\,s^{-1}$)

b the exponent of the moisture release equation depending on soil texture

b_l a soil texture parameter for layer l

B a dimensionless factor that has a theoretical range of 1/2 to $\pi/4$, it is assumed to be equal to 0.55 in this study

c_c specific heat of vegetation ($=2700\,J\,kg^{-1}\,K^{-1}$)

c_p specific heat of moist air, $c_p = c_{pd}(1 + 0.84q_a)$ ($J\,kg^{-3}\,K^{-1}$)

c_{pd} specific heat of dry air at constant pressure ($=1004.67\,J\,kg^{-1}\,K^{-1}$)

c_s specific heat of snow/ice ($=4200\,J\,kg^{-1}\,K^{-1}$)

c_{sp1} to c_{sp5} empirical parameters for snow dynamics, with the values of $1 \times 10^{-3}, 2.1 \times 10^{-2}, 1.5 \times 10^{-3}$, and 4.0×10^{-2} for c_{sp1} to c_{sp4}, respectively; and for c_{sp5}, it with values of 2 or 1 if melting is underway or not

c_w specific heat of water ($=4200\,J\,kg^{-1}\,K^{-1}$)

C_c heat capacity of canopy ($J\,m^{-2}\,K^{-1}$)

C_{ice} volumetric heat capacity of ice ($=2.05 \times 10^6\,J\,m^{-3}\,K^{-1}$)

C_s volumetric heat capacity of soil ($J\,m^{-3}\,K^{-1}$)

$C_{s,l}$ volumetric heat capacity of soil layer l ($J\,m^{-3}\,K^{-1}$)

E_g evaporation from the ground surface ($kg\,m^{-2}\,s^{-1}$)

$E_{g,s}$ sublimation from snow or ice on the ground surface ($kg\,m^{-2}\,s^{-1}$)

$E_{g,w}$ evaporation from puddled liquid water on the ground surface ($kg\,m^{-2}\,s^{-1}$)

E_i evaporation from the intercepted moisture ($kg\,m^{-2}\,s^{-1}$)

E_{ps} potential evaporation from the soil surface ($kg\,m^{-2}\,s^{-1}$)

E_s evaporation from the soil surface ($kg\,m^{-2}\,s^{-1}$)

E_{tr} vegetation transpiration ($kg\,m^{-2}\,s^{-1}$)

$E_{tr,l}$ the rate of water extraction from soil layer l in rooting zone by transpiration ($m\,s^{-1}$)

E_x soil controlled ex-filtration ($m\,s^{-1}$)

$f_{o,l}$ a volume fraction of organic matter in layer l (%)

$f_{r,l}$ a weighting function used in Eq. (30) and it is expressed as in Eq. (31)

F soil moisture flow flux ($m\,s^{-1}$)

F_b hydraulic flux through the bottom of model domain ($m\,s^{-1}$)

$F_{l-1,l}$, $F_{l,l+1}$ soil moisture flow fluxes between layers $l-1$ and l and between l and $l+1$, respectively ($m\,s^{-1}$)

$F_{0,1}$ hydraulic flux infiltrated to the underlying top soil layer from the surface ($m\,s^{-1}$)

G net energy flux at given interface ($W\,m^{-2}$)

G_c net energy flux at the canopy level (usually for changing canopy temperature, also termed canopy heat storage) ($W\,m^{-2}$)

$G_{l-1,l}$, $G_{l,l+1}$ conductive heat fluxes between layers $l-1$ and l and between layers l and $l+1$, respectively ($W\,m^{-2}$)

G_0 net energy flux at the ground surface under canopy (normally transmitted into soil layers) ($W\,m^{-2}$)

H sensible heat flux ($W\,m^{-2}$)

H_c sensible heat flux from the canopy to the boundary layer ($W\,m^{-2}$)

H_g sensible heat flux from the ground to the canopy and through it ($W\,m^{-2}$)

I_a actual infiltration ($m\,s^{-1}$)

I_{lim} the limiting value of infiltration rate after the time to ponding ($m\,s^{-1}$)

I_p the potential infiltration rate before ponding commences ($m\,s^{-1}$)

j the number that represents the soil constituents present in the layer, equal to 1–5 for liquid water, ice, minerals, organic materials, and air, respectively

k soil hydraulic conductivity ($m\,s^{-1}$)

k_l soil hydraulic conductivity of layer l ($m\,s^{-1}$)

$k_{l,l+1}$ soil hydraulic conductivity between layers l and $l+1$ ($m\,s^{-1}$)

k_{sat} the saturated hydraulic conductivity ($m\,s^{-1}$)

$k_{sat,l}$ the saturated hydraulic conductivity at layer l ($m\,s^{-1}$)

k_t thermal conductivity ($W\,m^{-1}\,K^{-1}$)

$K_{t,l}, k_{t,l-1}, k_{t,l+1}$ thermal conductivity of layers $l, l-1, l+1$, respectively ($W\,m^{-1}\,K^{-1}$)

$k_{t,l,j}$ thermal conductivity of a constituent j in layer l ($W\,m^{-1}\,K^{-1}$)

k_0 soil hydraulic conductivity corresponding to θ_0 (see Eq. (47)) ($m\,s^{-1}$)

l soil layer sequence number

LAI leaf area index ($m^2\,m^{-2}$)

LAI_{max} the maximum of LAI for specific land cover type ($m^2\,m^{-2}$)

LAI_{min} the minimum of LAI for specific land cover type ($m^2\,m^{-2}$)

LAI_{shade} leaf area index for shaded leaves ($m^2\,m^{-2}$)

LAI_{sun} leaf area index for sunlit leaves ($m^2\,m^{-2}$)

m a dimensionless factor used in Eq. (50), depends on soil texture, it is obtained from Stieglitz et al. (1997) and Campbell and Norman (1998)

M_{cb} standing mass of the composite biomass $= M_{cb,max}$ for trees; $= \gamma_{gi} \times M_{cb,max}$ for crops and grass ($kg\,m^{-2}$)

$M_{cb,max}$ the maximum standing mass of the composite biomass ($kg\,m^{-2}$)

M_{ci} the amount of intercepted moisture (rain or snow) on vegetation surfaces ($kg\,m^{-2}$)

$M_{ci,max}$ the maximum amount of interception (rain or snow) that can be stored on vegetation surfaces ($kg\,m^{-2}$)

$M_{ci,s}$ mass of snow or ice intercepted on the canopy ($\mathrm{kg\,m^{-2}}$)

$M_{ci,w}$ mass of water intercepted on the canopy ($\mathrm{kg\,m^{-2}}$)

M_{sp} weight of the overlying snow above a layer in per unit area ($\mathrm{kg\,m^{-2}}$)

$M_{wps,M}$, $M_{wps,m}$ parameters for the maximum and minimum liquid water holding capacity of a snow layer, 1.0×10^2 and $0.0\,\mathrm{kg\,m^{-3}}$, respectively ($\mathrm{kg\,m^{-3}}$)

M_{ws} liquid water holding capacity of a snow layer ($\mathrm{kg\,m^{-3}}$)

n number of soil layers within vegetation rooting depth

N number of soil layers considered within model domain

P precipitation ($\mathrm{m\,s^{-1}}$)

P_{int} the rate of intercepted moisture by the canopy ($\mathrm{m\,s^{-1}}$)

P_s percolate water supplied to the underlying soil layers ($\mathrm{m\,s^{-1}}$)

P_{su} water fluxes supplied into the soil layers, such as P_{un}, P_s, etc. ($\mathrm{m\,s^{-1}}$)

P_{un} precipitation rate at the ground surface ($\mathrm{m\,s^{-1}}$)

q_a specific humidity of the air above the canopy ($\mathrm{kg\,kg^{-1}}$)

r_a aerodynamic resistance for heat and water vapor fluxes above the canopy ($\mathrm{s\,m^{-1}}$)

$r_{a,u}$ aerodynamic resistance for heat and water vapor fluxes under the canopy ($\mathrm{s\,m^{-1}}$)

r_g ground surface resistance ($\mathrm{s\,m^{-1}}$)

r_l stomatal resistance at leaf level ($\mathrm{s\,m^{-1}}$)

$r_{l,sunlit}$ leaf stomatal resistance for sunlit leaves ($\mathrm{s\,m^{-1}}$)

$r_{l,shaded}$ leaf stomatal resistance for shaded leaves ($\mathrm{s\,m^{-1}}$)

R_n net absorbed radiation ($\mathrm{W\,m^{-2}}$)

R_{nc} net absorbed radiation by canopy ($\mathrm{W\,m^{-2}}$)

R_{ng} net absorbed radiation by under-canopy ground ($\mathrm{W\,m^{-2}}$)

R_{s_i} in-coming shortwave radiation ($\mathrm{W\,m^{-2}}$)

RH   air relative humidity (%)

s_w a source/sink term for water-per-unit time occurred at soil layers used in Eq. (34) ($\mathrm{m\,m^{-2}\,s^{-1}}$)

$s_{w,l}$ a source/sink term for water-per-unit time occurred at soil layer l, used in Eq. (37) ($\mathrm{m\,m^{-2}\,s^{-1}}$)

S_0 soil sorptivity ($\mathrm{m\,s^{-1/2}}$)

S_c a source (or sink) term for freezing or thawing of moisture stored on the canopy ($\mathrm{W\,m^{-2}}$)

S_e soil desorptivity ($\mathrm{m\,s^{-1}}$)

S_s a source (or sink) term for freezing or thawing of moisture occurred at soil layers ($\mathrm{W\,m^{-3}}$)

$S_{s,l}$ a source (or sink) term for freezing or thawing of moisture occurred at soil layer l ($\mathrm{W\,m^{-3}}$)

t, t_h time in units of seconds and hours, respectively

t_c corrected time of t_r (s)

t_p duration from the moment that rainfall event occurs till the moment ponding commences (s)

t_r a cumulative lasting time from the moment that rainfall event occurs (s)

T_a air temperature (K)

T_c canopy temperature (K)

T_g temperature of the underlying ground surface (K)

T_s, T_{sp} temperatures of soil and snowpack, respectively (K)

$T_{s,l}$ soil or snowpack temperature of layer l (K)

u wind speed ($\mathrm{m\,s^{-1}}$)

VPD   the vapor pressure deficit (mbar)

z depth from the surface of ground or snowpack if it is present (m)

z_l^{top}, z_l^{bottom} depth of the top and bottom of layer l (m)

z_p depth of pond on the soil surface (m)

z_r vegetation rooting depth (m)

z_{ref} a reference height within the atmospheric boundary layer (m)

Greek letters

β_z solar zenith angle (arc)

γ the psychometric constant ($=0.646 + 0.0006 \times (T_a - 273.13)$) ($\mathrm{J\,kg^{-1}\,K^{-1}}$)

γ_{gi} growth index $= (\mathrm{LAI} - \mathrm{LAI_{min}})/(\mathrm{LAI_{max}} - \mathrm{LAI_{min}})$

δt computing time step (s)

δT_s temperature change in soil layer l during computing time step δt (K)

$\delta \theta_l$ volumetric liquid water content change in soil layer l during computing time step δt ($\mathrm{m^3\,m^{-3}}$)

Δ the rate of change of the saturated water vapor pressure with temperature ($\mathrm{mbar\,K^{-1}}$)

θ soil volumetric liquid water content ($\mathrm{m^3\,m^{-3}}$)

θ_i initial liquid water content ($\mathrm{m^3\,m^{-3}}$)

θ_l soil volumetric liquid water content of layer l ($\mathrm{m^3\,m^{-3}}$)

$\theta_{l,j}$ volumetric fraction of a constituent j in layer l ($\mathrm{m^3\,m^{-3}}$)

θ_0 water content extending from the wetting front to the soil surface ($\mathrm{m^3\,m^{-3}}$)

λ latent heat of vaporization ($\mathrm{J\,kg^{-1}}$)

λ_c the macroscopic capillary length (m)

λ_v the latent heat of vaporization of water dependent on air temperature ($=(2.501 - 0.0024 \times (T_a - 273.13))$) ($\times 10^6\,\mathrm{J\,kg^{-1}}$)

λ_s latent heat of sublimation at $0\,^\circ\mathrm{C}$ ($=2.83 \times 10^6$) ($\mathrm{J\,kg^{-1}}$)

λ_w latent heat of vaporization (vapor:liquid) dependent on air temperature ($=(2.501 - 0.0024 T_a) \times 10^6$) ($\mathrm{J\,kg^{-1}}$)

λE latent heat flux ($\mathrm{W\,m^{-2}}$)

λE_c latent heat flux from the canopy to the boundary layer ($\mathrm{W\,m^{-2}}$)

λE_g latent heat flux from the ground to the canopy ($\mathrm{W\,m^{-2}}$)

λE_i evaporative latent heat flux from the intercepted moisture to the boundary layer ($\mathrm{W\,m^{-2}}$)

λE_{ip}	potential evaporative latent heat flux from the intercepted moisture ($W\,m^{-2}$)
λE_l	latent heat flux from the individual leaves to the boundary layer ($W\,m^{-2}$)
$\lambda E_{l,shade}$	latent heat flux from the shaded leaves to the boundary layer ($W\,m^{-2}$)
$\lambda E_{l,sun}$	latent heat flux from the sunlit leaves to the boundary layer ($W\,m^{-2}$)
λE_{tr}	transpirative latent heat flux from the canopy to the boundary layer ($W\,m^{-2}$)
ρ_a	density of air (=$1.225\,kg\,m^{-3}$ at $15\,^{\circ}C$)
ρ_{ice}	density of ice (=$920\,kg\,m^{-3}$)
ρ_{ns}	density of fresh snow ($kg\,m^{-3}$)
$\rho_{s,l}$	soil bulk density of layer l ($kg\,m^{-3}$)
ρ_{sp}	density of snowpack ($kg\,m^{-3}$)
ρ_{spd}	threshold of snow density used in Eq. (23) (=$1.5 \times 10^2\,kg\,m^{-3}$)
ρ_{spe}	threshold of snow density used in Eq. (20) (=$2.0 \times 10^2\,kg\,m^{-3}$)
ρ_w	density of water ($kg\,m^{-3}$)
τ_d	daylength (s)
φ	local slop angel (arc)
Φ	the pore volume fraction (total porosity) of soil ($m^3\,m^{-3}$)
Φ_b	the soil bubbling pressure (m)
Φ_l	the pore volume fraction (total porosity) of layer l ($m^3\,m^{-3}$)
ψ	soil moisture suction (potential) (m)
ψ_l	soil moisture suction at layer l (potential) (m)
ψ_f	soil moisture suction (metric head) at the wetting front (m)
ψ_l	soil moisture suction of layer l (m)
ψ_{max}	the critical soil moisture at which transpiration effectively ceases (wilting point; depending on plants species, generally equals 150 m)
ψ_{sat}	effective saturated soil moisture suction (m)
$\psi_{sat,l}$	effective saturated soil moisture suction at layer l (m)
ψ_0	soil moisture suction (metric head) corresponding to θ_0 (see Eq. (36)) (m)
Ω	foliage clumping index

separation of vegetation from soil and the inclusion of multiple soil layers for dynamic heat and moisture-flow simulations. In recent decades, the interactions among soil, vegetation and climate have been studied intensively and modeled successfully on the basis of water and energy transfer in the soil–vegetation–atmosphere system (e.g., Sellers et al., 1986; Dickinson et al., 1986; Verseghy, 1991; Verseghy et al., 1993; Cox et al., 1999; Wang et al., 2002a,b; Zhang et al., 2003). Also the construction and refinement of these kinds of models have received increasing attention (e.g., Sellers et al., 1996, 1997; Viterbo and Beljaars, 1995; Peart and Curry, 1998; Friend et al., 1997; Christopher and Ek, 2004). Some important parameters, such as land cover type (LC), leaf area index (LAI) are usually prescribed in the existing LSMs (Wang et al., 2002a). This kind of parameterization based on invari-

ant response surfaces, the use of "guesstimates", as well as missing dependencies between eco-physiological processes and boundary conditions impacted by climate change are the major shortcomings of the current LSMs (Christopher and Ek, 2004; Schwalm and Ek, 2001; Clark et al., 2001; Kickert et al., 1999; Kley et al., 1999).

Remote sensing techniques, which inherently have the ability to provide spatially comprehensive and temporally repeatable information of the land surface, may be the only feasible way to obtaining data needed for land surface and ecological process modeling (Graetz, 1990; Sellers et al., 1996; Kite and Pietroniro, 1996; Rango and Shalaby, 1999; Liu et al., 2003). The most common rationale for interfacing remote sensing and land surface-ecosystem models is using remotely sensed data as model inputs (Plummer, 2000). These input data, corresponding to forcing functions or state variables in ecological modeling (Jørgensen, 1994), include LC, LAI, normalized difference vegetation index (NDVI), and the fraction of photosynthetically active radiation (f_{PAR}). The exist approaches have taken part of these parameters to drive models (e.g., Running and Coughlan, 1988; Sellers et al., 1996; Chiesi et al., 2002; Loiselle et al., 2001). Another effort is the direct estimation of gross/net primary productivity (e.g., Goetz et al., 1999; Seaquist et al., 2003), of biomass (e.g., Bergen and Dobson, 1999; Bénié et al., 2005; Seaquist et al., 2003) and of plant growth (Maas, 1988; Kurth, 1994), by making use of f_{PAR} and NDVI. It has been shown that the direct estimation has lower accuracy than the integration of remotely sensed data with process based models (Goetz et al., 1999).

We developed a LSM based on remote sensing in this study, which is named as ecosystem–atmosphere simulation scheme (EASS). In addition to using LC, LAI, a foliage-clumping index (Ω), generated from satellite data, is first time applied to LSMs. In EASS, Ω is used to calculate the fraction of sunlit and shaded leaves and then to characterize the effects of three-dimensional canopy structure on radiation, water, and carbon fluxes.

It is realized that the exchanges of water and heat at the vegetated land surface are linked in nature to exchanges of CO_2 (Sellers et al., 1997; Wang et al., 2002b). In our effort in understanding the impact of climate change on terrestrial ecosystems and on global carbon balance, energy, water, and carbon cycles need to be modeled simultaneously (Sellers et al., 1996; Hutjes et al., 1998; Williams et al., 2001). Recently, LSMs have thus been enhanced to include the CO_2 flux between the land surface and the atmosphere, such as SiB2 (Sellers et al., 1996), IBIS (Foley et al., 1996), NCAR-LSM (Bonan, 1995), BATS (Dickinson et al., 1998) and CLASS-C (Wang et al., 2002b), though most of the ecosystem carbon processes developed in current LSMs are still relatively simple. In this study, the effects of climate, vegetation, ground features on hydrological and carbon dynamics are quantified and integrated on the basis of energy, water and carbon transfer in the soil–vegetation–atmosphere system. When we coupled the newly developed LSM (i.e., EASS) with an ecosystem model named boreal ecosystem productivity simulator (BEPS) (Chen et al., 1999; Liu et al., 1999, 2002), the simulation realism and accuracy in carbon dynamics are enhanced significantly. Moreover, realistic simulations in the surface sensible heat flux are critical for modeling the planetary boundary layer

(PBL). By coupling the EASS model with an atmospheric transport model (vertical diffusion scheme: VDS), we are able to achieve a greater degree of realism in simulated diurnal and seasonal variation of CO_2 than had previously been possible (Chen et al., 2004, 2005a, 2006a,b, 2007; Chen and Chen, 2007). Overall, this process-based land surface scheme (EASS) has the following characteristics: (i) satellite data are used to describe the vegetation phenology, type, structure (clumping) and density; (ii) energy and water exchanges and carbon assimilation in the soil–vegetation–atmosphere system are fully coupled and are simulated simultaneously. In energy flux estimation, we modified the "big-leaf model" by stratifying sunlit and shaded leaves, to be consistent with the photosynthesis-conductance model; (iii) snow and soil simulations are emphasized by including a flexible and multiple layering scheme. The EASS model has been tested and validated against multiple-year observed data at several sites. We on purpose calibrate and validate this model in 30-min time steps, using multiple-year continuous observations at sites in the southern study area of the Boreal Ecosystem–Atmosphere Study (BOREAS) because the majority of the existing LSMs have been validated under PILPS for short periods under temperate or warm climate (Henderson-Sellers et al., 1995; Chen et al., 1997; Saunders et al., 1999; Gustafsson et al., 2003). Moreover, EASS has been coupled with an atmospheric general circulation model named GEM (Côté et al., 1998a,b). This paper intends to describe this model formulation and a suite of offline tests for multiple-year periods. We focus on comparisons with measured latent and sensible heat fluxes that represent aggregated areal fluxes. However, comparisons with observed temporal variations at individual sites (soil temperature, soil water content, and stand transpiration) are also presented, since these contribute to an understanding of improvements and limitations in the present LSM. Results of coupling EASS to GEM, application of EASS to Canada's landmass, spatial scaling issues, performance of the coupled EASS-BEPS model in improving carbon flux estimation, are reported in Chen et al. (2007).

2. Model description

2.1. Outline of the model

EASS is based on a single vegetation canopy overlying a seven-layer soil, including physically based treatment of energy and moisture fluxes from the vegetation canopy and through it. It also incorporates explicit thermal separation of the vegetation from the underlying ground. Similar to some former models (e.g., Dickinson et al., 1986; Toconet et al., 1986; Tjernatrom, 1989), EASS treats the vegetation cover as a single layer (Thom and Oliver, 1997) rather than lumping it together with the ground. Moreover, EASS includes a scheme with stratification of sunlit and shaded leaves to avoid shortcomings of the "big leaf" assumption (De Pury and Farquhar, 1997; Liu et al., 2003). It has been referred as a "two-leaf" canopy model (Norman, 1980; Chen and Coughenour, 1994; Chen et al., 1999; Liu et al., 1997, 1999, 2002, 2003). Canopy and soil parameters, as model inputs, are derived from satellite imagery and a database of soil textural properties (Shields et al., 1991). EASS follows and

further develops the algorithms embedded in FOREST-BGC (Running and Coughlan, 1988) to describe the physical and biological processes in vegetation. With spatially explicit input data on vegetation, meteorology and soil, EASS can be run pixel by pixel over a defined domain, such as Canada's landmass, or any of its parts, or the globe. Similar to BESP (Liu et al., 2003), it has flexible spatial and temporal resolutions, as long as the input data of each pixel are defined.

The overall model structure is shown in Fig. 1. We considered the vertical profile of soil, vegetation (if present) and the atmosphere as an integrated system with two interfaces. In EASS, the energy balance and water balance are coupled, and both of them are discussed separately at two levels: canopy and underlying ground (Fig. 1). In compromise with limitations of available spatial data, we assume that environmental and plant conditions are horizontally uniform within the finest simulation unit (pixel) and lateral interactions among pixels are negligible. Thermal and moisture dynamics therefore can be determined by vertical energy and water fluxes. To accommodate using satellite data as model inputs, a single vegetation layer is considered in EASS, and yet the multi-layer scheme for energy exchanges and water transfers through the soil profile and the snowpack (if present) is introduced into EASS. The number of snow and soil layers and the depth of each layer are user-defined according to soil physical structures distributed in the profile and application objectives and so forth. The number of snow layers is adjusted according to snow depth. In the current study, the soil profile, including forest floor (if it is forest), organic layers, and mineral soil layers, is divided into seven layers and the thickness of the layers increases exponentially from the top layer to the sixth layer (equals to 0.05, 0.1, 0.2, 0.4, 0.8, and 1.6 m, respectively). The first six soil layers with a total depth of 3.15 m are set to ensure the complete simulation of energy dissipation in the soil column. The division of soil layers is applied to the snowpack if present. The total depth of snowpack is updated at every computing time step. When the thickness of snowpack is thinner than 5 cm, it is treated as part of the first soil layer and is weighted to obtain the grid cell values.

EASS is forced by near-surface weather variables at a reference level z_{ref} within the atmospheric boundary layer, including air temperature, relative humidity, in-coming shortwave radiation, wind speed, and precipitation. Some parameters of vegetation, such as LC, LAI, and Ω, are also generated from satellite data using the algorithms developed by Chen and Cihlar (1996) and Chen et al. (2002, 2003, 2005b). LAI is updated every 10 days to capture phenology, and Ω can also be made time varying when there will be sufficient multiple angle remote sensing data in the near future.

The most important parameter is LC as it is required in defining other land surface parameters. These parameters include vegetation height, canopy roughness length, canopy zero plane displacement, standing mass, leaf-angle distribution factor, ground roughness length, and rooting depth, etc. The land cover type for each pixel is identified as 1 of 10 classes based on the original 31 classes in Cihlar et al. (1999). The 10 classes include coniferous forest, mixed forest (mixture of coniferous and deciduous forest), deciduous forest, shrub land, burned area, barren land, cropland, grassland, urban area, and permanent snow/ice area. The land
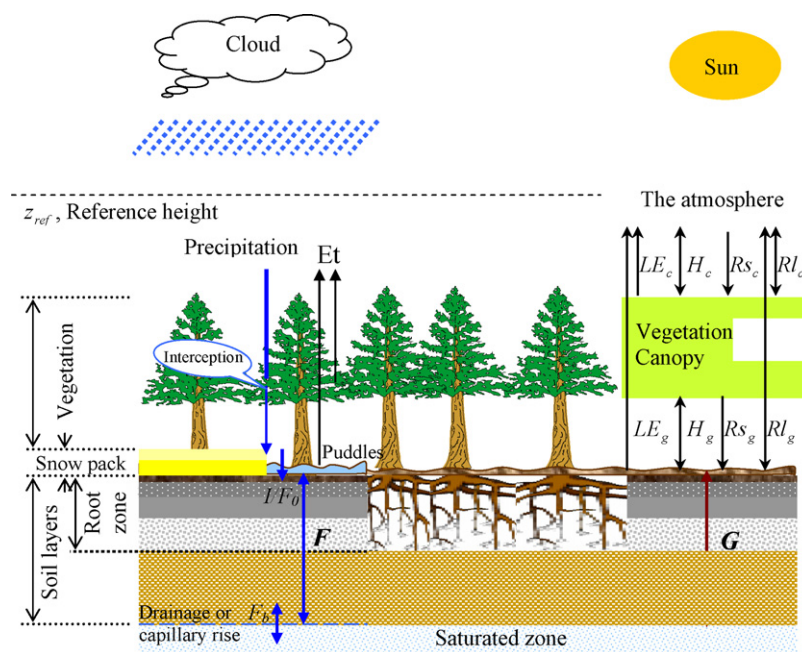
Fig. 1 – Structure of the EASS model. Three components (soil, vegetation and the atmosphere) are considered in EASS, which are integrated with two interfaces. The right panel illustrated energy fluxes between these three components. LE, H, Rs, Rl, and G are the latent heat flux, sensible heat flux, shortwave radiation, longwave radiation, and soil conductive heat flux, respectively; the subscripts g and c present the energy fluxes at soil–canopy and canopy–atmosphere interfaces, respectively. The left panel describes soil water fluxes. The symbol F represents conductive water flux between soil layers, and F_0 represents the incoming water flux from the surface to the top soil layer (i.e. the actual infiltration rate I), and F_b is the water exchange (drainage or capillary rise) between the bottom soil layer and the underground water.

cover map of Canada is generated to provide an up-to-date, spatially and temporally consistent national coverage. The data source is the advanced very high resolution radiometer (AVHRR) onboard NOAA 14 satellite.

Soil texture is crucial to soil properties, such as soil water content at saturation (porosity), soil water potential at saturation, soil thermal and hydraulic conductivities at saturation, etc. we classified soil texture into 11 categories in EASS following Campbell and Norman (1998), Rawls et al. (1992), and Kucharik et al. (2000). Data on soil texture (silt and clay fraction) are obtained from the Soil Landscapes of Canada (SLC) database, the best soil database currently available for the country (Shields et al., 1991; Schut et al., 1994; Tarnocai, 1996; Lacelle, 1998). The soil textural data for each EASS layer are directly from SLC version 2.0 (Tarnocai, 1996; Lacelle, 1998). To generate these data layers with the same projection and resolution as for other datasets, the original vector data in SLC are joined, reprojected and rasterized using the ArcGIS geographic information system.

2.2. Energy balance and thermal dynamics

2.2.1. Energy balance equations
In general, the surface energy balance at any physical surface can be described as Eq. (1) (the equations are listed in Table 1, and the definitions of the variables are listed in Nomeclature). The vegetation cover and the under-canopy ground are treated as different layers in EASS. Similar to some former models (Tjernatrom, 1989; Verseghy et al., 1993), we assume

that heated air rising from the ground below vegetation cannot pass through the canopy without warming it but water vapor rising from the ground can pass through the canopy without condensing on the foliage (Fig. 1). So the energy balance at canopy–atmosphere and soil–atmosphere (under the canopy) interfaces can be expressed as Eqs. (2) and (3), respectively.

Boreal forests are typically highly clumped. We modified 'the one-larger vegetation model' to calculate radiation transfer and interception with stratification of sunlit and shaded leaves for estimating energy fluxes, to be consistent with the photosynthesis conductance model. This consistency is found to be particularly important when transpiration is used as an additional constraint on estimation of gross primary productivity of a stand. The net absorbed radiation calculations in EASS for the canopy (R_{n_c}) and the under canopy ground surface (R_{n_g}) are discussed in Appendix A.

The sensible heat flux is modeled using the bulk aerodynamic approach. The sensible heat fluxes from the canopy to the boundary layer and from the ground to the canopy are calculated using Eqs. (4) and (5), respectively. The estimation of aerodynamic resistance is discussed in Appendix B.

The transpirational latent heat flux at the leaf level ($\lambda_w E_l$) is estimated on the basis of Penman–Monteith equation (Monteith and Unsworth, 1965) (Eq. (6)) for sunlit and shaded leaves separately. The leaf stomatal resistance for water vapor (r_l, in $s\,m^{-1}$) in Eq. (6) is calculated using a modified version of the Ball–Woodrow–Berry (Ball et al., 1987) empirical model. The r_l for sunlit ($r_{l,sunlit}$) and shaded ($r_{l,shaded}$) leaves is explicitly constrained by their leaf net photosynthesis assimilation

Table 1 – Equations used in the model

Energy balance

$$0 = G + R_n + \lambda E + H \tag{1}$$

$$0 = G_c + R_{n_c} + H_c + \lambda E_c - H_g \tag{2}$$

$$0 = G_0 + R_{n_g} + H_g + \lambda E_g \tag{3}$$

$$H_c = \frac{\rho_a c_p (T_a - T_c)}{r_a} \tag{4}$$

$$H_g = \frac{\rho_a c_p (T_c - T_0)}{r_{a,u}} \tag{5}$$

$$\lambda E_l = \left[\frac{\Delta R n_c + \rho c_p VPD / r_a}{\Delta + \gamma (1 + r_l / r_a)} \right] \tag{6}$$

$$\lambda E_c = \lambda_{w/s} E_i + \lambda_w E_{tr} \tag{7}$$

$$\lambda E_i = \min(\lambda_{w/s} E_{ip}, \lambda_{w/s} M_{ci}) \tag{8}$$

$$\lambda E_{tr} = \lambda_w E_{l,sun} LAI_{sun} + \lambda_w E_{l,shade} LAI_{shade} \quad (\text{when } M_{ci} = 0) \tag{9}$$

$$LAI_{sun} = 2 \cos \beta_z \left[1 - \exp \left(\frac{-0.5 \Omega LAI}{\cos \beta_z} \right) \right] \tag{10a}$$

$$LAI_{shade} = LAI - LAI_{sun} \tag{10b}$$

Thermal dynamic of canopy and soil profile

$$C_c \frac{\partial T_c}{\partial t} = G_c + S_c \tag{11}$$

$$C_c = c_c M_{cb} + c_w M_{ci,w} + c_s M_{ci,s} \tag{12}$$

$$C_s \frac{\partial T_s}{\partial t} = \frac{\partial}{\partial z} \left(k_t \frac{\partial T_s}{\partial z} \right) + S_s \tag{13}$$

$$\frac{C_{s,l} \delta T_{s,l}}{\delta t} = \frac{G_{l-1,l} - G_{l,l+1}}{D_l + S_{s,l}} \quad (l = 1, 2, 3, \ldots, N-1) \tag{14}$$

$$G_{l-1,l} = G_{0,1} = G_0 \quad (l = 1) \tag{15}$$

$$G_{l-1,l} = \frac{(0.5 k_{t,l-1} + 0.5 k_{t,l})(T_{s,l-1} - T_{s,l})}{(0.5 D_{l-1} + 0.5 D_l)} \quad (l = 2, 3, 4, \ldots, N) \tag{16}$$

$$C_{s,l} = \sum_{j=1}^{5} C_{l,j} \theta_{l,j} \tag{17}$$

$$C_{s,l} = \frac{2.0 \times 10^3 \rho_{s,l}}{2.65} + 4.2 \times 10^6 \theta_{l,w} + 2.5 \times 10^6 f_{o,l} \tag{18}$$

$$k_{t,l} = \prod_{j=1}^{5} k_{t,l,j}^{\theta_{l,j}} \tag{19}$$

Snowpack and its dynamics

$$M_{wsp} = \max \left(M_{wsp,m} (M_{wsp,M} - M_{ws,m}) \frac{\rho_{spe} - \rho_{sp}}{\rho_{sp}} \right) \tag{20}$$

$$\rho_{ns} = \max(50, (50 + 1.7(T_a - 258.13)^{1.5})) \tag{21}$$

$$\frac{\partial \rho_{sp}}{\partial t_h} = \rho_{sp} c_{sp1} \exp(-0.08(273.13 - T_{sp})) M_{sp} \exp(-c_{sp2} \rho_{sp}) \tag{22}$$

$$\frac{\partial \rho_{sp}}{\partial t_h} = \begin{cases} c_{sp5} c_{sp3} \rho_{sp} \exp(c_{sp4}(T_{sp} - 273.13)) & (\rho_{sp} \le \rho_{spd}) \\ c_{sp5} c_{sp3} \rho_{sp} \exp(c_{sp4}(T_{sp} - 273.13)) \times \exp[4.6 \times 10^{-3} (\rho_{spd} - \rho_{sp})] & (\rho_{sp} > \rho_{spd}) \end{cases} \tag{23}$$

$$C_{sp} = \frac{C_{ice} \rho_{sp}}{\rho_{ice}} \tag{24}$$

$$k_{t,sp} = 2.576 \times 10^{-6} \rho_{sp}^2 + 0.074 \tag{25}$$

Moisture regime

$$M_{ci,max} = a_v LAI \tag{26}$$

$$P_{int} = \begin{cases} P[1 - \exp(-\Omega LAI)] & (M_{ci} < M_{ci,max}) \\ 0 & (M_{ci} = M_{ci,max}) \end{cases} \tag{27}$$

$$P_{un} = P - P_{int} \tag{28}$$

$$M_{ci}(t) = \min([M_{ci}(t-1) + (P_{un} \rho_{w/ns} - E_{i,c}) \delta t], [M_{ci,max}]) \tag{29}$$

$$E_{tr,l} = \frac{f_{r,l} E_{tr}}{\rho_w} \tag{30}$$

$$f_{r,l} = \frac{\theta_{l,r} [\psi_{max} - \psi_l]}{\sum_{l=1}^{n} \theta_{l,r} [\psi_{max} - \psi_l]} \tag{31}$$

$$\theta_{l,r} = \frac{\exp(-3.0 z_l^{top}) - \exp(-3.0 z_l^{bottom})}{1 - \exp(-3.0 z_r)} \tag{32}$$

$$F = k \left(\frac{\partial \psi}{\partial z} + 1 \right) \tag{33}$$

$$\frac{\partial \theta}{\partial t} = \frac{\partial F}{\partial z} + s_w = \frac{\partial}{\partial z} \left[k \left(\frac{\partial \psi}{\partial z} + 1 \right) \right] + s_w \tag{34}$$

Table 1 (Continued)

$$k = k_{sat} \left[\frac{\theta}{\Phi} \right]^{(2b+3)} \tag{35}$$

$$\psi = \psi_{sat} \left[\frac{\theta}{\Phi} \right]^{-b} \tag{36}$$

$$\frac{\delta\theta_l}{\delta t} = \frac{F_{l-1,l} - F_{l,l+1} - E_{tr,l}}{D_l} + s_{w,l} \quad (l = 1, 2, 3, \ldots, N) \tag{37}$$

$$F_{l-1,l} = \frac{k_{l-1,l}(\psi_{l-1} - \psi_l)}{(0.5D_{l-1} + 0.5D_l) + k_{l-1,l}} \quad (l = 2, 3, 4, \ldots, N-1) \tag{38}$$

$$k_{l-1,l} = \left[\frac{k_{l-1}\psi_{l-1} + k_l\psi_l}{\psi_{l-1} + \psi_l} \right] \left[\frac{b_{l-1} + b_l}{b_{l-1} + b_l + 6} \right] \quad (l = 2, 3, 4, \ldots, N-1) \tag{39}$$

$$F_{l,l+1} = F_b = \sin\varphi\, k_{sat,l} \left(\frac{\theta_l}{\Phi_l} \right)^{(2b+3)} + 0.001 \left(\frac{\theta_{sat,l}D_l}{\tau_d} \right) \left(\frac{\theta_l}{\Phi_l} \right) \quad (l = N) \tag{40}$$

$$F_{l-1,l} = F_{0,1} = \begin{cases} \min[(P_{un} - E_s/\rho_w + P_s), I_p] & (z_p = 0) \\ I_{lim} & (z_p > 0) \end{cases} \quad (l = 1) \tag{41}$$

$$\frac{\partial z_p}{\partial t} = \frac{P_{un} - E_s}{\rho_w} + \frac{P_s - I_a - E_{g,w}}{\rho_w} \tag{42}$$

$$I_p = \frac{k_0(\psi_0 - \psi_f)(\theta_0 - \theta_i)}{P_{su} - k_0} \tag{43}$$

$$I_{lim} = S_0 t_c^{1/2} \tag{44}$$

$$\psi_f = \frac{\lambda_c}{2B} \tag{45}$$

$$S_0 = \frac{[(\theta_0 - \theta_i)(k_0 - k_i)\lambda_c]^{1/2}}{B} \tag{46}$$

$$t_c = t_r + \frac{I_p - (\psi_0 - \psi_f)(\theta_0 - \theta_i)\ln((1 + I_p)/(\psi_0 - \psi_f)(\theta_0 - \theta_i))}{k_0} - t_p \tag{47}$$

$$E_s = \min(E_{ps}, E_x) \tag{48}$$

$$E_s = S_e t^{-1/2} \tag{49}$$

$$S_e = \rho_w \left[\frac{8\Phi k_{sat}\Phi_b}{3(1 + 3m)(1 + 4m)} \right]^{1/2} \left[\frac{\theta}{\phi} \right]^{(m/2+1)} \tag{50}$$

(see Appendix B) because the photosynthesis rate for sunlit and shaded leaves can be very different due to their differences in radiation interception and the leaf surface micro-environmental conditions (Chen et al., 2007). The transpirational latent heat and vegetation water exchange are consequently coupled to carbon dynamics. The transpirational latent heat flux of the canopy ($\lambda_w E_{tr}$) is the sunlit and shaded LAI weighted sum of the leaf-level $\lambda_w E_l$ (Eq. (9)). The total canopy latent heat flux is the sum of evaporative latent heat flux (λE_i) and canopy transpirational latent heat flux ($\lambda_w E_{tr}$) (Eq. (7)). The intercepted water in the canopy is consumed by the evaporative latent heat flux. λE_i is estimated as the minimum of the potential evaporative heat flux (λE_{ip}, using Eq. (6) by changing r_l to 0, and selecting λ_w or λ_s for liquid water or snow, respectively) and the amount of intercepted water (rain or snow) on vegetation surfaces (M_{ci}, see Section 2.5.1) (Eq. (8)). We simply assume that transpiration is subject to evaporation of the intercepted water. The transpirational latent heat flux ($\lambda_w E_{tr}$) is calculated using Eq. (9) from individual sunlit and shaded leaves. It is noted that this value calculated using Eqs. (6) and (9) is the potential transpiration. The actual transpiration E_{tr} is controlled by both of the climate and the soil water conditions. Transpiration consumes water in the root zone and is subject to the amount of available soil water for plant uptake (i.e., above the wilting point). The partitioning of total tree LAI into sunlit and shaded portions is a function of Ω and cosine of solar zenith angle (β_z) (Eq. (10)) (Norman, 1982; Chen et al., 1999). The latent heat flux from the ground (λE_g) is estimated on the basis of Penman–Monteith equation (Monteith and Unsworth, 1965) (Eq. (6)) by replacing the leaf stomatal resistance with the

ground surface resistance, which is a function of soil moisture (Sun, 1982). r_g is set to $0\,s\,m^{-1}$ when the surface is covered by snow.

2.2.2. Thermal dynamics of canopy and soil profile

2.2.2.1. Canopy temperature. The change in canopy temperature can be calculated using Eq. (11). An internal heat source or sink term S_c for freezing or thawing of moisture stored on the canopy (see Section 2.4) is considered as well. The heat capacity of vegetation (C_c) in Eq. (11) is a weighted sum of the standing mass in the canopy and intercepted water or/and snow on the canopy (using Eq. (12)).

2.2.2.2. Heat conduction in soil profiles. The thermal dynamics of the soil profile is determined by numerically solving the one-dimensional (vertical direction) heat conduction equation (Eq. (13)). An internal heat source or sink term (Patankar, 1980) is included in the equation as well. Convective heat transfer with water flow is not considered in the model. Eq. (13) is solved numerically by converting it to an explicit form (Eqs. (14)–(16)) for more efficient calculation. The time steps of 30 min or less are used in the model so that the calculation is stable. The heat capacity ($C_{s,l}$) of a soil layer l is calculated from the heat capacities ($C_{l,j}$) of liquid water, ice, minerals, organic materials, and air present in the layer, weighted according to their respective volumetric fractions θ_j (Eq. (17)). In case of no ice present in a layer, the soil volumetric heat capacity $C_{s,l}$ of layer l can be calculated with reasonable accuracy from the volumetric water content $\theta_{l,w}$ and the soil bulk density $\rho_{s,l}$ by Eq. (18) with a volume fraction $f_{o,l}$ of organic matter (Hillel, 1980a,b). The thermal conductivity of soil layer is determined

following the method of Johansen (1975), as recommended by Farouki (1981) (Eq. (19)). To solve the heat conduction equation (Eq. (13)), we need to define the upper and lower boundary conditions. The net energy flux at the ground surface under canopy (G_0 in Eq. (3)) is assumed to be transmitted into soil layers as the upper boundary condition (Eq. (14)). It is assumed that the temperature remains almost constant at the damping depth (D_h). In other words, D_h is a constant characterizing the decrease in amplitude with increasing distance from the soil surface. It is defined as $(2T_d/\omega)^{1/2}$, where ω is the frequency of a temperature fluctuation. For annual fluctuation $\omega = 2\pi/365\,\mathrm{day}^{-1}$. The thermal diffusivity T_d is the change in temperature produced in a unit volume by the quantity of heat flowing through the volume in unit time under a unit temperature gradient. It can be calculated from thermal conductivity (k_t) and volumetric heat capacity (C_s) as $k_t(\rho C_s)^{-1}$. At a depth $z = \pi D_h$, the phase difference is π from the surface, i.e., the temperature wave is exactly out of phase with the wave at the surface (Monteith and Unsworth, 1990). Different from most LSMs which set adiabatic condition as the lower boundary condition, e.g., SIB (Masayuki and Takayuki, 2004), we treat the soil layer at depth of $0.5\pi D_h$ as a temperature-constant layer. The soil temperature of this layer is set equal to a value of the annual average air temperature at the height of z_{ref}.

2.3. Snowpack and its dynamics

In the EASS model, the thermal regime of the snowpack is distinguished from that of the underneath soil if its thickness is greater than 5 cm. The snowpack is modeled as a part of the profile for heat conduction, using the same equations for thermal dynamics in Section 2.2.2. Snowfall is determined by precipitation and air temperature. The amount of snow intercepted by the vegetation canopy and lost through sublimation is discussed in Section 2.5.1. The thickness of snowpack is calculated on the basis of the amount of snow (water equivalent) and snow density on the ground. The amount of snow is the balance of snowfall and snowmelt. The amount of snowmelt is estimated on the basis of the available energy. We define the snowpack temperature of layer l solved by Eq. (13) without considering the thawing/freezing effects (assume $S_{s,l} = 0$) as apparent temperature $T'_{s,l}$. If $T'_{s,l} > 0\,°C$, energy is available for snowmelt. $T_{s,l}$ is then reset to $0\,°C$. In this case, the fluxes affected by surface temperature are recalculated, and the excess energy is assumed to be available for snowmelt. The melted water at layer l will percolate to a deeper layer if the liquid water content of this layer exceeds its holding capacity (Anderson, 1976). The liquid water holding capacity of a snow layer is calculated following Kongoli and Bland (2000) using Eq. (20). If this case occurs at the bottom layer of the snowpack profile, the percolating water will be supplied to the underlying soil. This water may infiltrate into soil or accumulate on soil surface depending on percolating rate (P_s) and the infiltration capacity (see Section 2.5.2). The density of fresh snow is estimated depending on air temperature with a threshold of $-15\,°C$ following LaChapelle (1969) (Eq. (21)). The change of snow density in each layer is simulated considering compaction (Eq. (22)) (Mellor, 1977) and destructive metamorphism (Eq. (23)) (Anderson, 1976; Kongoli

and Bland, 2000). The effects of liquid water is also considered by the parameter (c_{sp5}) in Eq. (23) (Kongoli and Bland, 2000; Anderson, 1976). The heat capacity of a snow layer is estimated from the heat capacity of ice and the densities of snow and ice (Eq. (24)). The effective of thermal conductivity of each snow layer is determined from ρ_{sp} using Eq. (25) fitted to field measurements presented in Mellor (1977). The thickness of snowpack is updated every day on the basis of the amount of snow (water equivalent) and its density profile.

2.4. Thawing and freezing

It is assumed that thawing or freezing occurs when temperature crosses $0\,°C$ if there is available ice or water. The internal heat source or sink term (or latent heat of fusion) (S_c in Eq. (11) or S_s in Eq. (13)) is considered if thawing or freezing occurs. The thawing or freezing of water in soil and intercepted by canopy is simulated in a similar way as for snowmelt. The amount of thawing or freezing at each computing time step is estimated on the basis of the amounts of available energy and ice/snow or water. If there is water (rain or snow) stored on vegetation canopy surfaces ($M_{ci} > 0$) (see Section 2.5.1), the canopy temperature calculated using Eq. (11) without considering thawing and freezing processes is called apparent temperature, T'_c. The effects of thawing or freezing on the apparent temperature are calculated based on energy conservation. Latent heat released or absorbed during freezing or thawing must equal the amount of heat required for the canopy apparent temperature change to reach a "new" (actual) energy balance. All the energy fluxes in Eq. (2) are re-computed by replacing T'_c with T_c. For the case of thawing ($M_{ci,s} > 0\,\mathrm{kg\,m}^{-2}$ and $T'_c > 0\,°C$), if the available heat ($C_c(T'_c - 0)$) is less than thawing all the snow/ice storage on the canopy ($M_{ci,s}$), the canopy temperature is set to $0\,°C$, and $M_{ci,s}$ is reduced according to the available energy; otherwise all the ice will be melted and the remaining heat will be used to increase canopy temperature. A similar procedure is conducted for the freezing case.

We model the thawing and freezing processes in the soil profile in a similar way as for canopy. Soil volumetric water content (θ) is updated using Eq. (37) (see Section 2.5.2). The fractions of liquid water and ice in a layer are explicitly determined and the heat capacity of the soil is estimated at each time step according to the fraction of liquid water and ice content. The depth of thawing or freezing is determined on the basis of the fractions of liquid water and ice in soil layers (Zhang et al., 2003).

2.5. Moisture regime

2.5.1. Moisture storage on the canopy and evapotranspiration

It is assumed that precipitation is either rainfall or snowfall with a separating threshold of air temperature at $0\,°C$ (Kongoli and Bland, 2000). Precipitation arriving at the vegetation canopy is either intercepted by foliage or falls to the ground through gaps in the canopy. The maximum amount of interception (rain or snow) that can be stored on vegetation surfaces ($M_{ci,max}$), the rate of interception by the canopy (P_{int}), and precipitation rate at the ground surface (P_{un}), depend on

a number of factors, such as vegetation type, canopy architecture, LAI, Ω, precipitation intensity, and wind speed, etc. However, field observations reported in the literature indicate that they are mainly determined by LAI and Ω. The simple relationship (Eqs. (26) and (27)) works well for both rain and snow and for a wide variety of vegetation types and precipitation events. Vegetation interception proceeds with the rate P_{int}, and the excess precipitation falls through gaps in the canopy to the ground with the rate P_{un} until $M_{ci,max}$ is reached. After this point, all the precipitation reaches the ground (Eq. (28)). The actual amount of intercepted moisture (rain or snow) on vegetation surfaces (M_{ci}) is the balance of P_{int} and E_i (Eq. (29), selecting ρ_w or ρ_{ns} for rainfall or snow, respectively).

As discussed above, the evapotranspiration from the canopy is assumed, for the sake of simplicity, to deplete the interception first, since the associated resistance is less. When the intercepted water has been exhausted by evaporation, transpiration consumes water from the soil layers in the root zone. We introduce Eq. (30) to partition the total actual transpiration (E_{tr}) (see Section 2.2.1) into the rate of water extraction from each soil layer l in the rooting zone ($E_{tr,l}$) (Verseghy et al., 1993; Feddes et al., 1974). A weighting function $f_{r,l}$ in Eq. (30) is defined on the basis of the fraction volume of roots $\theta_{l,r}$ and the soil moisture suction ψ_l in that layer (Eq. (31)). By assuming that $\theta_{l,r}$ at the ground surface and at vegetation rooting depth z_r equal to 1 and 0, respectively, $\theta_{l,r}$ can be estimated using Eq. (32). When no snowpack and no puddles are present, soil evaporation E_s (see Section 2.5.2) occurs and consumes water from the top layer first, and then proceeding through underlying layers.

2.5.2. Soil water dynamics

Water movement in soils occurs under both saturated and unsaturated conditions (Fig. 1). Saturated conditions occur below the water table where water movement is predominately horizontal. In compromise with limitations of available spatial data, we adjust the water table as the bottom of model domain for soil water transfer calculation if the water table is higher than the bottom of model original domain. Similar to most LSMs (e.g., NEST, Zhang et al., 2003), water vapor movement and liquid water movement in response to temperature gradients are ignored. Water movement in soils obeys Darcy's law. Water fluxes between unsaturated layers are simulated using the modified Darcy's equation by Buckingham (1907) for unsaturated flow (Eq. (33)). The change in soil volumetric water content θ is determined by numerically solving the one-dimensional Richards equation (Eq. (34)) (Richards, 1931). The hydraulic conductivity k and soil moisture suction ψ are estimated on the basis of soil volumetric water content and soil texture (Eqs. (35) and (36)) (Campbell, 1974; Clapp and Hornberger, 1978). k_l is set to zero when the simulated temperature for this layer is below 0 °C (Williams and Smith, 1989). The parameters (b, Φ, k_{sat} and ψ) are determined by soil texture. These parameters are estimated on the basis of statistically derived relationships with soil texture presented in Cosby et al. (1984) and Clapp and Hornberger (1978) for mineral soils, and Ogee and Brunet (2002) and Letts et al. (2000) for forest floor and peat layers, respectively.

Eqs. (33) and (34) are solved numerically by converting them to the explicit forms of Eqs. (38) and (37), respectively, for efficient calculations. The hydraulic conductivity between two layers is estimated using weighting methods on the basis of these two layer's moisture suctions (Milly and Eagleson, 1982). We modify Milly and Eagleson's equation with specific b values of these two layers (Eq. (39)).

To solve the one-dimensional Richards equation (Eq. (34)), we need to define the upper and lower boundary conditions. The drainage of water out of the bottom of the soil column as the lower boundary condition is given by Eq. (40) (Sellers et al., 1996). For our 1D model water lateral flow is ignored therefore the local slop angle φ equals 0 in Eq. (40). The upper boundary condition is controlled by the actual infiltration rate I_a from the surface to soil layers and actual evaporation E_s which ex-filtrates water from soil layers. The model currently assumes a flat landmass with no runoff on the ground. In the case the surface water supply (e.g., rainfall) exceeds I_a, we assume that a puddle occurs. Under conditions when there is no puddle on the soil surface, the surface condition is determined by both of the water "supply fluxes" (such as rainfall, irrigation, E_s, etc.) and the potential infiltration I_p. Otherwise, under ponded condition I_a is subject to the infiltration capacity I_{lim} (Eq. (41)). The depth of ponding z_p is estimated on the basis of water equivalent equation (Eq. (42)). Both of the I_p (before ponding commences) and I_{lim} (after ponding t_p) are controlled by soil hydraulic properties (Hillel, 1980a,b). During the early stages of a rainfall event before ponding occurs, the infiltration rate is estimated based on a simplified equation first proposed by Green and Ampt (1911) as implemented by Mei and Larson (1973) (Eq. (43)). After ponding, the actual infiltration rate is calculated using Eq. (44) following Philip (1957). The macroscopic capillary length is determined by soil physical properties (Eq. (45)). The soil sorptivity and the corrected time in Eq. (44) are estimated using the method of Radcliffe and Rasmunssen (2000) with Eqs. (46) and (47), respectively. In case there is no water supply (e.g., precipitation, irrigation, puddled water, etc.), the surface upper boundary condition is switched to evaporation E_s from soil surface. E_s is subject to both the potential evaporation E_{ps} (also called climate-controlled) and the soil-controlled exfiltration rate F_s. E_s is calculated using Eq. (48) following Eagleson (1978). E_{ps} is estimated using Eq. (6) by replacing leaf stomatal resistance with soil surface resistance, F_s is calculated using the method of Entekhabi and Eagleson (1989) (Eqs. (49) and (50)).

3. Dataset for model tests and evaluation

EASS model tests have been conducted for Canada's landmass using gridded meteorological variables, and EASS has been coupled with an atmospheric general circulation model GEM (Chen et al., 2007). Offline model tests with a 30-min time step for multiple years were done by comparing with the field measurements at two sites in Canada.

3.1. Site descriptions

Both of the sites used for EASS calibration are located at the Southern Study Area of BOREAS, Saskatchewan, Canada.

One site (53.6°N, 106.20°W) is covered by deciduous forest of aspen (*Populus tremuloides*), with an understorey dominated by hazelnut (*Corylus cornuta*) (hereafter refer to the OA site). The overstorey has an even age (~70 years old) with a mean canopy height of 21.5 m and a stem density of 860 stems ha^{-1}. Previous glacial erosion left the region with a gently rolling topography. This site is moderately well drained. Another site (53.92°N, 104.69°W) is a coniferous forest of jack pine (*Pinus Banksiana*) (hereafter refer to the OJP site).

We selected these two sites because of detailed data for model validation. The measurements made for these two towers are outlined as follows. Half-hourly eddy correlation flux measurements of sensible heat, latent heat, and CO_2 fluxes were made above and under the canopy using a triple-axis Applied Technology sonic anemometer and an infrared absorption spectrometer. Photosynthetically active photon flux density and the net radiation balance were measured above the forest with a quantum sensor (LiCor model LI-190S) and a net radiometer (Swissteco Model S-1 or REBS model 6), respectively. Meteorological variables were also measured and stored as half-hour averages to coincide with the flux measurements. Half-hourly averaged soil temperatures were measured with two multi-level thermocouple probes. Sensors were spaced logarithmically at 2, 4, 8, 16 and 32 cm below the surface at the OJP site, while at depths of 2, 5, 10, 20, 50, and 100 cm at the OA site. Whereas the soil water content was measured at 4 h intervals at depths of 0–15, 15–30, 30–60, 60–90 and 90–120 cm. Further detailed descriptions and measurements about these two sites are reported by Black et al. (1996), Blanken et al. (1997), and Baldocchi et al. (1997a,b).

3.2. Dataset for model inputs

The multiple-year continuous meteorological variables observed above the canopy at these two sites are used to drive EASS. But vegetation parameters (i.e., LC, LAI) are derived from satellite images at 1-km resolution (directly from AVHRR images, or up-scaling from Landsat TM) instead of directly using observed canopy data. Soil properties for these two select sites are obtained from SLC database version 1.0 and 2.0 (Tarnocai, 1996; Lacelle, 1998). Vegetation foliage clumping significantly alters its radiation environment and therefore
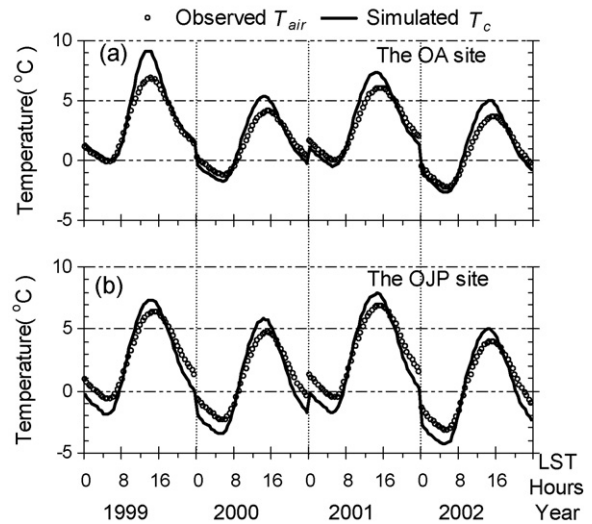

Fig. 2 – **Annually averaged diurnal composites of simulated canopy temperature (T_c) and observed air temperature (T_{air}) above the canopy. (a) and (b) are for the OA site and the OJP site, respectively.**

affects water and heat as well as carbon cycle. The clumping index Ω quantifies the level of foliage grouping with distinct canopy structures, such as tree crowns, shrubs, and row crops, relative to a leaf spatial random distribution. Mapping of Ω for Canada's landmass is approached using multi-angular POLDER 1 data on a methodology documented by Chen et al. (2005b).

3.3. Dataset for comparisons

The observed energy fluxes at the sites, such as net radiation, latent and sensible heat fluxes are used to compare with model outputs. The simulated fluxes represent aggregated areal fluxes around the tower. We also made comparisons of measured soil temperature, soil water content, and evapotranspiration with model simulation, though these observations represent smaller areas than the simulations which represent areal averages surrounding the observation tower (around 1 km^2).

Table 2 – Regression results between modeled and observed half-hourly energy fluxes at OA and OJP sites during 1999–2002[a]

	OA site						OJP site					
	r^2			RMSE (W m^{-2})			r^2			RMSE (W m^{-2})		
	R_n	λE	H	R_n	λE	H	R_n	λE	H	R_n	λE	H
1999	0.95	0.71	0.83	37.3	39.7	35.7	0.89	0.70	0.74	26.4	20.4	29.7
2000	0.92	0.63	0.66	94.3	49.6	88.7	0.91	0.64	0.81	34.3	25.3	23.8
2001	0.94	0.75	0.70	35.5	28.6	38.4	0.88	0.73	0.78	26.1	21.7	26.4
2002	0.91	0.73	0.72	30.4	30.7	41.2	0.92	0.69	0.79	26.9	23.2	24.3

[a] r^2 is the squared linear regression coefficient; RMSE is the root mean square error $= \sqrt{1/n \sum_{i=1}^{N} [C_{mod}(i) - C_{obs}(i)]^2}$. The sample number is the maximum of 17,520 with 5–15% reduction of missing observed data.
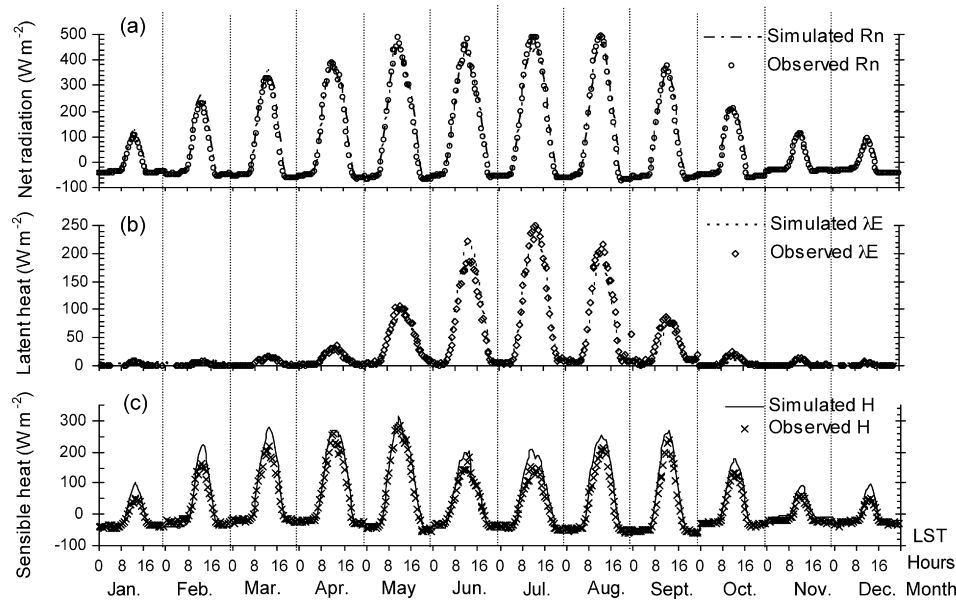
Fig. 3 – Monthly averaged diurnal composites of modeled and observed energy fluxes for the year 2001 at the OA site. (a) Net radiation (R_n); (b) latent heat (λE); (c) sensible heat (H).
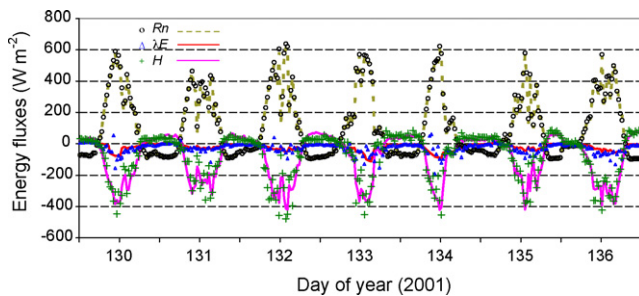
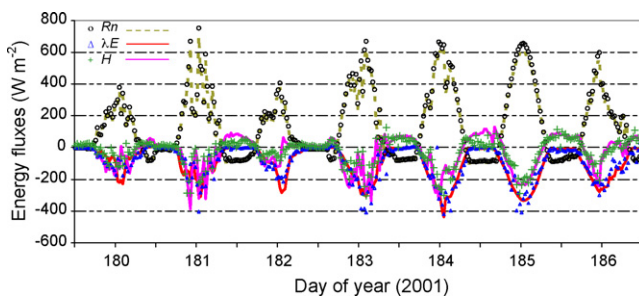

Fig. 4 – Simulated (lines) and tower measured (symbols) half-hourly fluxes of net radiation (R_n), sensible heat (H), and latent heat (λE) over the canopy in the early growing season in 2001 at the OA site; H and λE are positive downwards conveniently.

4.   Results and discussion

4.1.   Synoptic and diurnal scales

The diurnal variations in canopy temperature are well simulated for these two sites as shown in Fig. 2. Canopy temperature is higher than air temperature at mid-day, while lower at nighttime. The EASS model's performance in simulating the diurnal variation for different seasons is quite reasonable with regard to energy fluxes. The results of regression analyses between the simulated and measured half-hourly energy fluxes at these two sites during 1999–2002 are list in Table 2. Analyses against averaged monthly composite diurnal data for R_n, λE and H (monthly averaged half-hourly values) at OA site during 1999–2002 (sample number $n = 2304$) show that, the squared correlation coefficient r^2 equals 0.9875, 0.9332, and 0.9275 for R_n, λE and H, respectively; and the corresponding RMSE (root mean square error) equals to 19.23, 15.72,

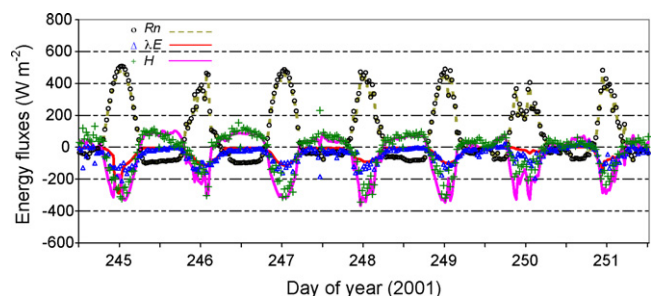
Fig. 5 – Simulated (lines) and tower measured (symbols) half-hourly fluxes of net radiation (R_n), sensible heat (H), and latent heat (λE) over the canopy in the mid-growing season in 2001 at the OA site; H and λE are positive downwards conveniently.

Fig. 6 – Simulated (lines) and tower measured (symbols) half-hourly fluxes of net radiation (R_n), sensible heat (H), and latent heat (λE) over the canopy in the late growing season in 2001 at the OA site; H and λE are positive downwards conveniently.
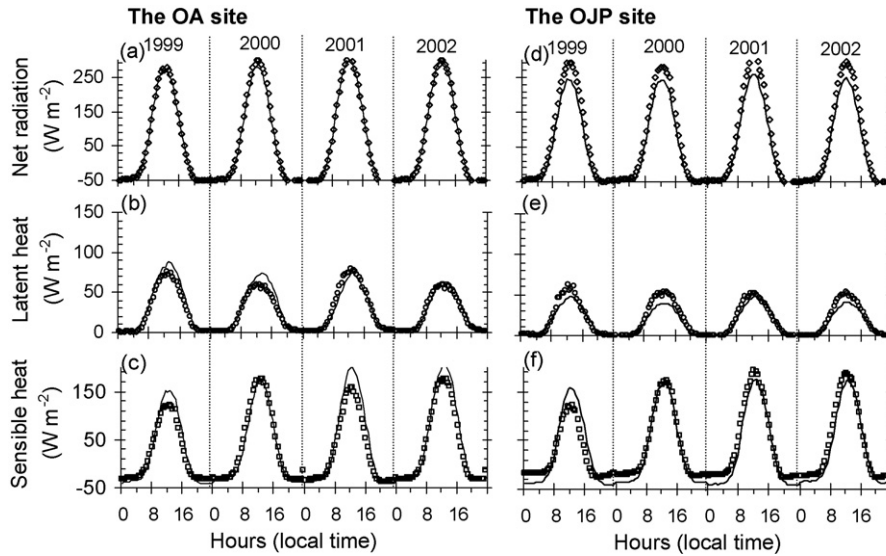
Fig. 7 – Annually averaged diurnal composites of simulated and observed energy fluxes during 1999–2002, at both OA and OJP sites. In all plots, model results are shown with lines, while observations with symbols. (a)–(c) are for net radiation (R_n), latent heat (λE), and sensible heat (H) for the OA site, respectively; (d)–(f) are same as (a)–(c), respectively, but for the OJP site.

and 28.29 W m^{-2}, respectively. Fig. 3 is shown as an example for the OA site during the year 2001. Simulated R_n and λE agree well with observations for the whole year, while modeled H is overestimated to some degree, especially during winter and

spring seasons. Similarly, the regression analyses against the monthly composite diurnal course (monthly averaged half-hourly values) at OA site in 2001 ($n = 576$) show that, r^2 equals 0.9962, 0.966, and 0.9716, and RMSE equals 11.56, 10.59 and
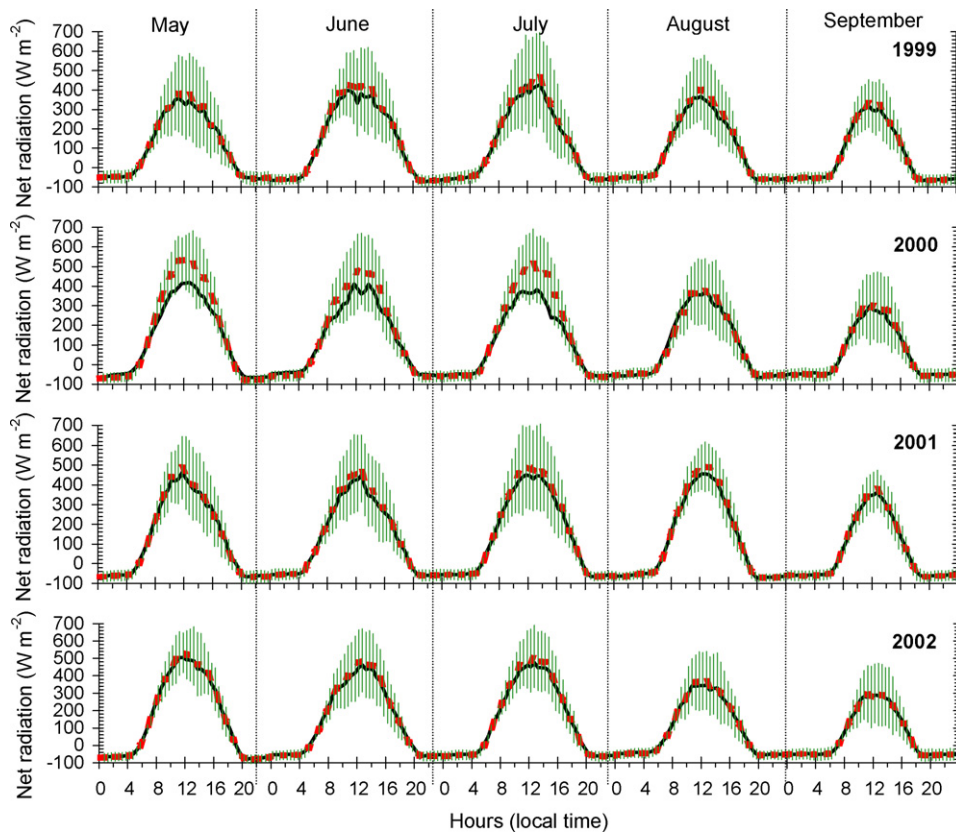

Fig. 8 – Diurnal composites of modeled and observed net radiation in the growing season during 1999–2002 at the OA site. In all plots, model results are shown with solid lines, while observations dashed line. The bars indicate ±1 standard deviation of the mean of the observations.

28.05 W m^{-2}, for R_n, λE and H, respectively. Seasonal variability in the diurnal amplitude in both modeled and observed λE is more obvious than that in H. Diurnal amplitudes of both modeled and observed λE are much smaller before and after growing season (January to April and October to December) than during the growing season (May to September).

Half-hourly plots of modeled and measured R_n, H, and λE over the canopy for three separate weeks in 2001 at the OA site are shown in Figs. 4–6, which are selected to cover the model response in different phases of the growing season (early, middle and late) and under different weather conditions (clear, cloudy and rainy). Because of the presence of plant stems and branches, land surface albedo in the deciduous forest still remains low even if the ground surface is covered by snow (Betts and Ball, 1997) in the early growing season when LAI is small. The woody area index (WAI) influences both solar radiation and longwave radiation. By considering a WAI of 0.5 in the radiation balance calculations in the EASS model, the simulated R_n is improved over the runs in which radiation interception by wood is absent. The radiation energy received by the canopy during daytime is mainly dissipated as H. As shown in Fig. 4, simulated R_n and H capture the observed variation with no obvious bias in the week of mid-May. Under clear weather conditions, simulated R_n and H reach the values of 600 and 400 W m^{-2}, respectively (days 132–134), similar to measured values. The regression analyses between the simulated and measured half-hourly R_n and H during this week ($n = 336$) show that, r^2 equal 0.9964 and 0.9088, while RMSE

equal 15.24 and 43.66 W m^{-2}, respectively. Both observed and simulated λE values during this week are very small ($r^2 = 0.393$ and RMSE = 24.34 W m^{-2}). In the week in early July (Fig. 5), both modeled and simulated λE increase remarkably and exceed H in most days. This seasonal shift in energy partitioning will be discussed in Section 4.2. The agreement between modeled and observed λE during this week improves significantly compared to those in the earlier growing season and is also better than H simulation in this week ($r^2 = 0.8544$, RMSE = 35.25 W m^{-2} for λE, and $r^2 = 0.8109$, RMSE = 40.73 W m^{-2} for H, respectively). The modeled R_n follows the observed extremely well under diverse weather conditions ($r^2 = 0.9987$, RMSE = 19.43 W m^{-2}) during the mid-growing season. Both modeled and observed H values exceed λE again in the late growing season, particularly around noontime (Fig. 6). This suggests that energy partition may be constrained by available soil water contents. The squared correlation coefficients r^2 for R_n, H, and λE are 0.9991, 0.8761, and 0.4266, respectively; and the corresponding RMSE equal 12.06, 41.66 and 30.47 W m^{-2}, respectively.

Overall, modeled energy fluxes at half-hourly time steps agree with tower measurements well (Table 2). The simulated R_n is close to the observations, while both λE and H are slightly overestimated. As mentioned above, the energy fluxes are calculated with stratification of sunlit and shaded leaves in EASS, to avoid shortcomings of the "big-leaf" assumption. Model experiments shows that the simulation realism and accuracy in R_n, H and λE by the new strategy are enhanced about 9–14% compared with the "big-leaf model" (i.e., the RMSE decrease
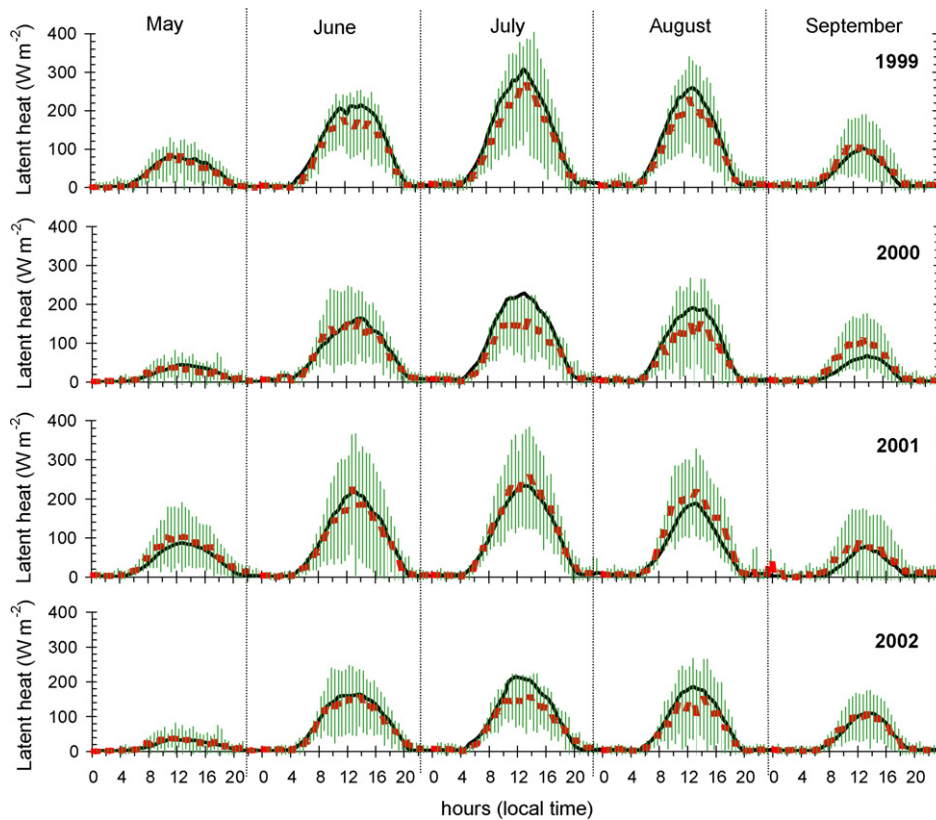

Fig. 9 – Diurnal composites of modeled and observed latent heat (λE) in the growing season during 1999–2002 at the OA site. In all plots, model results are shown with solid lines, while observations dashed line. The bars indicate ±1 standard deviation of the mean of the observations.
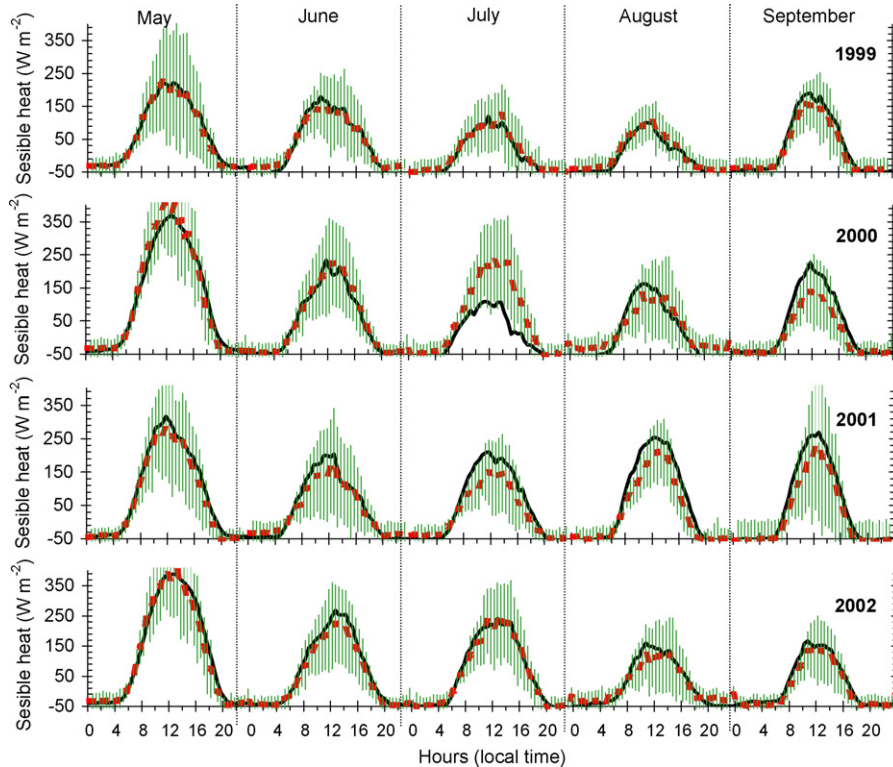
Fig. 10 – Diurnal composites of modeled and observed sensible heat (H) in the growing season during 1999–2002 at the OA site. In all plots, model results are shown with solid lines, while observations dashed line. The bars indicate ±1 standard deviation of the mean of the observations.

around 9% and 14% for the OA site and the OJP site, respectively). Moreover, the clumping index (Ω) is useful for accurate separation of sunlit and shaded leaves in the canopy. The RMSE for simulated energy fluxes increase about 5% and 8% for the OA site and the OJP site, respectively, if we exclude the effects of Ω on the radiation interception and the separation of sunlit and shaded leaves (i.e., let $\Omega = 1$ in Eq. (10a)).

To test EASS model performance in simulating diurnal variations across multiple years under different weather conditions, annual averaged diurnal courses are compared in Fig. 7. During the 4 years, the simulated diurnal variations in R_n closely trace observations for the OA site (Fig. 7a), but a systematic bias is found for the OJP site. The model underestimate R_n near mid-day (10:30–14:30 LST) by 15–30% (Fig. 7d). These biases suggest that either the land surface albedo is overestimated in the model at OJP site or the land surface parameters for this 1 km × 1 km grid box around the measurement tower derived from satellite images do not represent the footprint area of the tower observation. As mentioned before, the modeled λE is also underestimated by 10–20% compared to observations at this site. This is possibly due to the similar reason as for R_n simulation or suggests that the effects on evapotranspiration by the wetting factors may be underestimated in our model. The exception to this is the drought year 2001 (Fig. 7e; the precipitation of 2001 is less by 23% than the 4-year average, while the simulated λE values are close to observations in this year). These systematic biases may be possibly compensated by other unknown offsets in the year 2001. The diurnal variations in H are modeled well for this
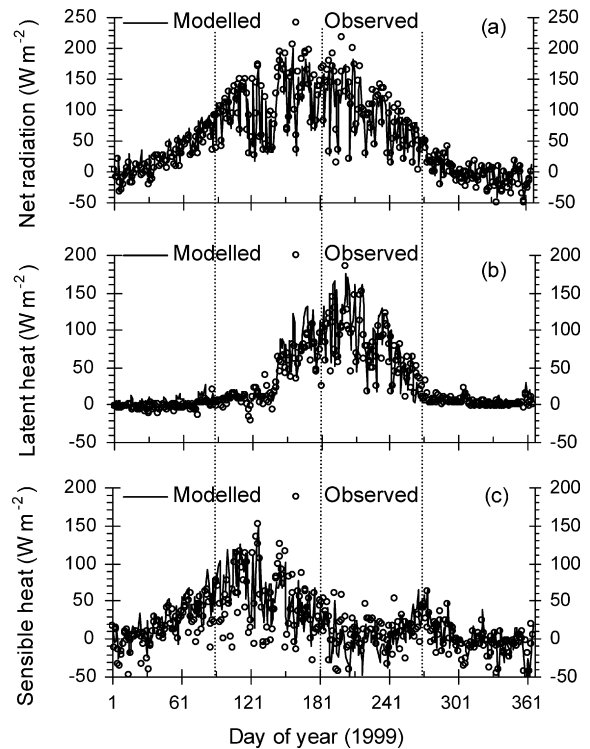

Fig. 11 – Annual patterns of simulated (line) and measured (symbols) daily energy fluxes for the year 1999 at the OA site. (a) Net radiation (R_n); (b) latent heat (λE); (c) sensible heat (H).
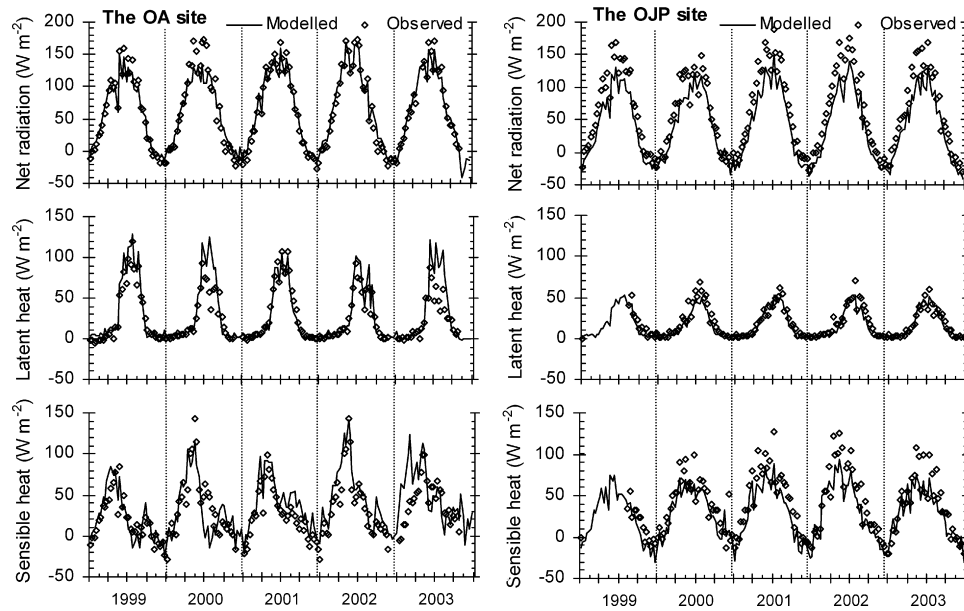
Fig. 12 – Simulated (line) and measured (symbols) energy fluxes (10-day averages) at these two sites during the years 1999–2003.

OJP site with an exception for the wet year 1999 (Fig. 7f). The model overestimates H during daytime (10:00–15:00 LST) by 10–20% in 1999 (the precipitation of 1999 is 20% higher than the 4-year average). Similar to the OJP site, systematic biases in simulating diurnal-variations in H and λE are also found for the OA site: around min-day the model overestimates λE in wet years (Fig. 7b) while overestimates H in drought years (Fig. 7c). The simulated diurnal peak value of λE (occurred during 10:00–14:00 LST) is higher than observation by 10–20% in 1999 and in 2000 (the precipitations of 1999 and 2000, respectively, are higher than the 4-year average by 29% and 30%). A similar situation occurs in H simulations for the drought years 2001 and 2002 (the precipitations are lower than the 4-year average by 37% for 2001 and by 23% for 2002, respectively). Both these modeled and observed diurnal amplitudes of H in drought years are higher than those in wet years (Fig. 7c and f), whereas λE in wet years is higher than that in drought years (Fig. 7b and e). This suggests that the forest is stressed in dry years affecting energy partition with low evapotranspiration.

During the growing season, energy fluxes reach their largest values of the year, especially λE, because moist soil, highest LAI and warm climate provide optimum conditions for plant transpiration. To explore the EASS model's response to different weather conditions during different phases of growing season, monthly averaged diurnal composites during the growing season for these 4 years at the OA site are compared in Figs. 8–10. The modeled R_n is consistent with measurement (Fig. 8). The model underestimates R_n for May, June and July during 2000 by 15–20%, but still within ±1 standard deviation range of the mean of the observations. Modeled λE and H capture the observed diurnal variation with no obvious bias for most of the 40 months. The exception to this is the wet year 2000: λE is overestimated while H is underestimated though they are still within or near the margins of ±1 standard devi-

ations (Figs. 9 and 10). This may suggest that the amount of intercepted rainfall by the canopy is overestimated by around 5–10% in our model.

4.2. Seasonal and inter-annual variability

The annual distributions of modeled daily energy fluxes (R_n, λE and H) for the year 1999 at the OA site, for example, are compared with daily measurements (Fig. 11). Regression analyses of the daily data for this year show that the values of r^2 and RMSE are 0.9623 and 13.1 W m^{-2} for R_n, 0.8953 and 15.3 W m^{-2} for λE and 0.7417 and 19.5 W m^{-2} for H, respectively. Both modeled and observed annual peak values of H occur in April and May (Fig. 11c), while annual peak values of λE are found in June and July (Fig. 11b) associated with the rainy season (Fig. 15). Most seasonal variations in daily energy fluxes are captured
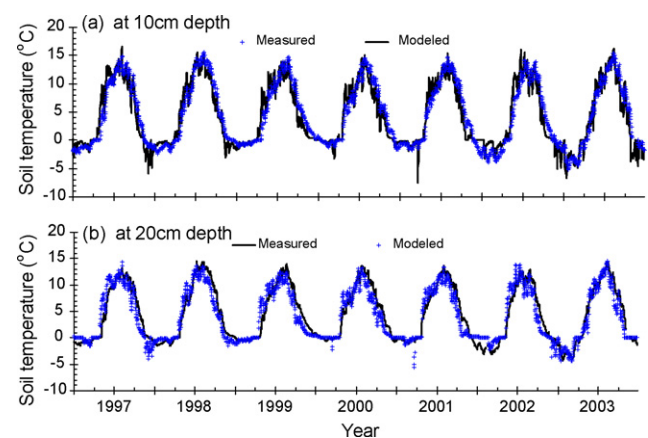

Fig. 13 – Simulated (line) and measured (symbols) daily soil temperature in model layers at (a) 10 cm and (b) 20 cm depths during 1997–2003 at the OA site.
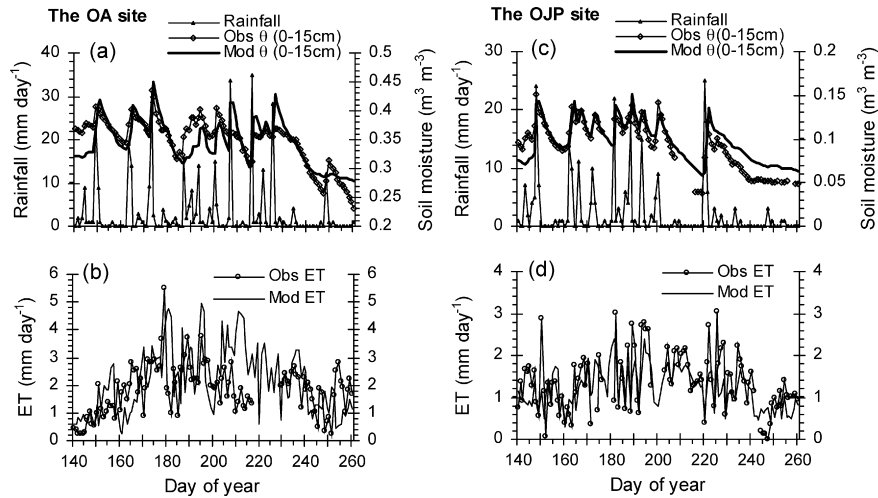
Fig. 14 – Simulated (Mod θ, solid line) and measured (Obs θ, dashed line with symbols) unfrozen soil moisture in the surface layer (0–15 cm deep) (daily averages) during the growing season of 2000 for these two sites (panels (a) and (c)). Modeled results are integrated over two top layers to match with the observations. Measured data for the OA site are averaged from two measured soil profiles at this site (panel (a)). Daily total rainfall (measured, panels (a) and (c)) and ET (both modeled and measured, panels (b) and (d)) are also shown as comparisons. Panels (a) and (b) for the OA site; while (c) and (d) for the OJP site.

by EASS though *H* is overestimated in March and April to some degree. This is possibly due to an inadequate representation of the moss layer in EASS (Fig. 11c). The simulated and measured energy fluxes (10-day averages) for both the OA site and the OJP site during 1999–2003 are shown in Fig. 12. Modeled R_n, λE and *H* agree closely with tower observations for these 5 years. At OJP site, R_n is systematically underestimated by 15–30% (the reasons for this have been discussed above), consequently resulting in a bias in modeled λE. The values of r^2 for R_n, λE, and *H* between the model and measurements are 0.9608, 0.8675, and 0.7819 for the OA site and 0.9425, 0.8808, and 0.8515 for the OJP site, respectively; the corresponding RMSE equals 12.7, 15.2 and 21.9 W m^{-2} for the OA site, and

25.0, 6.6 and 17.2 W m^{-2} for the OJP site, respectively. EASS performs well in simulating seasonal and inter-annual variability in energy fluxes (R_n, λE and *H*). As shown in Fig. 13, modeled soil temperature agrees with observations for the long term seasonal variations: the squared correlation coefficients r^2 between model and measurements ($n > 2500$) are 0.9043 and 0.8985 for the soil layer of 0–10 and 10–20 cm, respectively. The corresponding RMSE equals 1.77 and 1.81 °C, respectively.

To evaluate the performance and reliability of the model in simulating soil moisture dynamics at seasonal and inter-annual temporal scales, the key parameters (soil moisture contents, evapotranspiration, and rainfall) during the growing season for both the OA and OJP sites are compared in
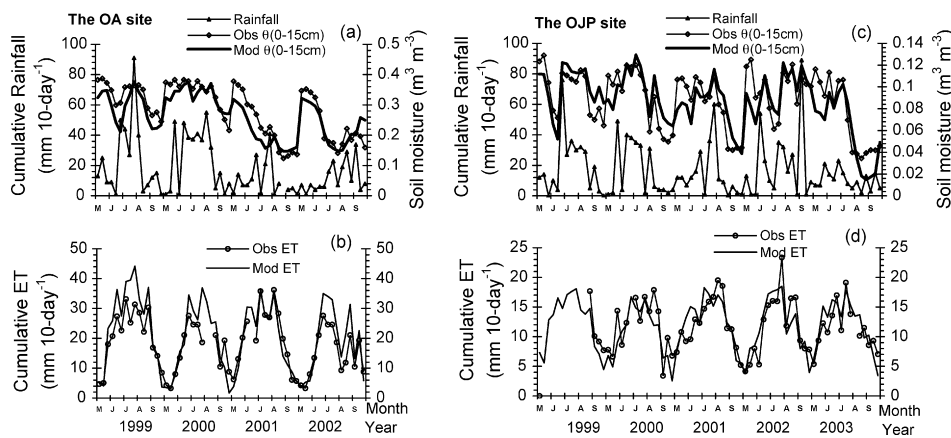

Fig. 15 – Simulated (Mod θ, solid line) and measured (Obs θ, dashed line with symbols) 10-day averaged soil moisture in the surface layer (0–15 cm deep) during the growing season, 1999–2002, for these two sites (panels (a) and (c)). Modeled results are integrated over two top layers to match with the observations. Measured data for the OA site are averaged from two measured soil profiles at this site (panel (a)). Ten-day total rainfall (measured, panels (a) and (c)) and ET (both modeled and measured, panels (b) and (d)) are also shown as comparisons. Panels (a) and (b) for the OA site; while (c) and (d) for the OJP site.

Figs. 14 and 15. The simulated soil moisture at the surface layer is close to measurements. The model has the ability to capture the inter-annual variations as well as the differences between these two sites. Simulated and measured soil moistures vary dramatically corresponding to rainfall events: the larger the amount of rainfall, the larger the increase in soil moistures. The effect of evapotranspiration on soil moistures is less than that of rainfall in boreal ecosystems. Both simulated and measured evapotranspiration from these two sites are most sensitive to the changes in temperature (not shown) and least sensitive to precipitation (Figs. 14 and 15).

5. Summary and conclusions

Land surface energy, water and carbon processes are closely linked in nature, and implementing them realistically and simultaneously in LSMs is important. In this study, a process based land surface scheme (EASS) using remote sensing data is developed and coupled to an ecosystem model BEPS, in which energy, water and carbon exchanges are fully integrated and are simulated simultaneously. Offline tests of the model are made against multiple-year, half-hourly tower measurements made at two boreal sites. Model parameters are not 'tuned' for each test site to obtain a better match with tower observations. Rather, model validations and experiments are designed to test the model performance for a location in which observed meteorological data are available, but which is otherwise not different from any other pixels. This paper focuses on presentations of energy and water modules while the carbon dynamics simulation will be reported elsewhere (Chen et al., 2007).

Offline tests indicate that the model can capture most of the physical processes occurring at the land surface at these two sites over diurnal, synoptic, seasonal and inter-annual time scales, such as surface energy exchanges, soil heat transfer, snow and thawing/freezing dynamics, canopy and soil temperatures, and soil moistures. However, considerable discrepancies between simulations and observations still occasionally exist, especially in λE and soil moistures as shown in Fig. 14. This is probably a result of several factors. Firstly, though the modeling strategy of sunlit and shaded leaf separation can effectively address the radiation distribution within the canopy and its impact on carbon fixation and energy partitioning and is an improvement from the "big-leaf" model, it is still rather simple compared with the real field conditions. Secondly, EASS behavior of evaporation from wet leaves is not tested since dew or frost observations are not available. There exists a combination of errors of resistance and soil moisture conductivity parameters in EASS. The transpirational latent heat and vegetation water exchange are dynamically coupled with carbon assimilation through $r_{l,\text{sunlit}}$ and $r_{l,\text{shaded}}$, thus inaccuracies in r_l estimation may be the main deficiency that led to discrepancies in the evapotranspiration simulation. Further model improvement on r_l calculation is imperative. Thirdly, the EASS model assumes uniform horizontal distribution of land surface conditions within the model grids (i.e., $1\,\text{km} \times 1\,\text{km}$), and the vegetation parameters (LC, LAI, and Ω) are derived from the remote sensing data at 1 km resolution, whereas the tower flux measurements represents the inte-

grated results of its footprint area, within which heterogeneity in vegetation and soil properties can be considerable. Finally, discrepancies could also be related to data quality.

Different from most existing LSMs, this remote sensing-based EASS model dynamically integrates energy, water and carbon exchanges at each time step with a 'two-leaves' formulation (separation of sunlit and shaded leaves) instead of a "big-leaf" method. This modeling strategy is implemented for the first time in a LSM. It has the advantage of being physically and biologically realistic. It can also be easily implemented in general circulation models (GCM) compared to the "multi-layer" approach. So far EASS has been coupled with an atmospheric general circulation model named GEM (see Chen et al., 2007).

The advance in the use of satellite data to describe spatial and temporal variations of vegetation parameters in EASS is also significant. Several previous LSMs used remote sensing data (e.g., Running and Coughlan, 1988; Sellers et al., 1996; Chiesi et al., 2002; Loiselle et al., 2001), which include f_{PAR}, NDVI, as well as simple estimates of LAI. Using LAI allows mechanistic simulations of various fluxes that cannot be achieved through using f_{PAR} or NDVI, and it has been suggested that the traditional use of f_{PAR} should be abandoned and replaced with LAI and Ω (Chen et al., 2003). The foliage-clumping index Ω is introduced, for the first time, into a LSM to characterize the effects of the three-dimensional canopy structure on radiation, energy and carbon fluxes. Model experiments show significant improvements in the simulation of energy and water dynamics after the introduction of Ω and the separation of sunlit and shaded LAI.

Multi-year simulation results (as shown in Figs. 14 and 15) and experiments of model sensitivity to the meteorological variables of air temperature and rainfall in the growing season show that evapotranspiration from these boreal ecosystems is most sensitive to the changes in temperature and least sensitive to rainfall, and the effect of evapotranspiration on soil moistures is less than that of rainfall.

Because snow and soil simulations are emphasized by including a flexible and multiple layer scheme, the model reasonably reproduced the general diurnal, seasonal and inter-annual patterns of the soil heat fluxes and soil temperatures observed at two boreal sites. But there exist significant biases in soil moistures simulations. This is probably a result of the model's simplification of surface runoff and lateral flow of ground water. In the cases of impermeable and or steeply sloping surface, overland flow will have to be allowed. Moreover, some parameters, such as the resistances of plant roots and soil, are not directly tested owing to the limitation of measurements.

LSMs coupled with GCMs need to be validated with different vegetation types under various climate conditions. Physiological mechanisms and interactions with environment conditions are different among different vegetation types, such as plants with different photosynthesis pathways (C3 versus C4). Further model tests for crops and grass are yet to be done. Another area of improvement still remains to be made in the model is water balance processes and soil water regime. For example, parameterizations need to be verified for the resistances of plant roots and soil, and new parameterizations are yet to be developed for overland runoff and

lateral ground-water flow, particularly in areas underlain by permafrost.

Appendix A. Algorithm for net radiation of vegetation and ground surface

In order to consist with BEPS, the methods used in BEPS for calculating visible radiation (Chen et al., 1999; Liu et al., 2003) are modified for total solar radiation calculation. The effects of different canopy architectures in different vegetation functional types on radiation balance are considered in the canopy radiation module of the EASS, in that the net radiation of the sunlit and shaded leaves is computed separately:

$$R_{n_c} = R_{n_{sun}} + R_{n_{shade}} \tag{A.1a}$$

$$R_{n_{sun}} = S^*_{sun} LAI_{sun} + L^*_{sun} \tag{A.1b}$$

$$R_{n_{shade}} = S^*_{shade} LAI_{shade} + L^*_{shade} \tag{A.1c}$$

where R_n, S and L represent net radiation, shortwave irradiance, and longwave radiation, respectively; the subscripts *sun* and *shade* denote the sunlit leaves and shaded leaves, respectively; superscript * denotes the absorbed radiation by sunlit or shaded leaves. Downward flux is defined as positive conventionally. The partitioning of total tree LAI into sunlit and shaded portions is a function of clumping index (Ω, a dimensionless parameter with a value ranging of 0–1), and cosine of solar zenith angle (β_z) (Chen et al., 1999; Norman, 1982). The partition of incoming solar radiation into direct and diffuse components (S_{dir} and S_{dif}) is made using Chen's empirical equations (Chen et al., 1999). The absorption of shortwave radiance by sunlit leaves (S^*_{sun}) and the mean shaded leaf irradiance (S^*_{shade}) are calculated based on Norman (1982).

Net longwave exchanges of sunlit and shaded leaves are treated as the same, i.e.:

$$L^*_{sun} = L^*_{shade} = L^*_c \tag{A.2}$$

A more elaborate formulation can be made to consider the temperature difference between sunlit and shaded leaves. However, our sensitivity tests suggested that the detailed calculations of leaf energy budget and temperature can make only less than 1% difference in canopy energy balance computing. The net longwave irradiances for the vegetation canopy

(L^*_c) is calculated using the following equation:

$$L^*_c = \varepsilon_c \sigma [\varepsilon_a T_a^4 + \varepsilon_g T_g^4 - 2\varepsilon_c T_c^4] \times \left[1 - \exp\left(\frac{-0.5 LAI \Omega}{\cos \bar{\theta}} \right) \right] \tag{A.3}$$

The absorbed radiation by the soil surface (R_{n_g}) includes two components: shortwave (S^*_g) and longwave (L^*_g). S^*_g is calculated as

$$S^*_g = [(1 - \alpha_{g,dir}) S_{dir} + (1 - \alpha_{g,dif}) S_{dif}] \exp\left(\frac{-0.5 LAI \Omega}{\cos \bar{\theta}} \right) \tag{A.4}$$

where $\alpha_{g,dir}$ and $\alpha_{g,dif}$ are the albedo of the ground surface for direct and diffuse radiation, respectively. L^*_g is computed from

$$L^*_g = \varepsilon_g \varepsilon_a \sigma T_a^4 \exp\left(\frac{-0.5 LAI \Omega}{\cos \bar{\theta}} \right)$$
$$+ \varepsilon_g \varepsilon_c \sigma T_c^4 \left[1 - \exp\left(\frac{-0.5 LAI \Omega}{\cos \bar{\theta}} \right) \right] - \varepsilon_g \sigma T_g^4 \tag{A.5}$$

where σ is Stefan–Boltzmann constant, and equals $5.67 \times 10^{-8} \, W \, m^{-2} \, K^{-4}$; T represents temperature, in K; ε is emissivity; the subscripts a, c, and g represent the atmosphere, vegetation canopy, and ground surface, respectively. Pre-described values of 0.98 and 0.95 are assigned to ε_c and ε_g, respectively, according to Chen and Zhang (1989) and Chen et al. (1989). ε_a is computed using $\varepsilon_a = 1.24 (e_a/T_a)^{1/7}$ (Brutsaert, 1982), where e_a is water vapor pressure in mb.

Appendix B. Calculation for aerodynamic resistance and stomatal resistance

B.1. Aerodynamic resistance above the canopy

The turbulent transfer processes above the vegetation canopy are different from those below the canopy, while the turbulent transfer processes between the canopy and the reference height (z_{ref}) are assumed to be constant. The aerodynamic resistance r_a for heat and water vapor fluxes above the canopy is calculated using similar algorithms in CLASS (Verseghy et al., 1993).

B.2. Aerodynamic resistance below the canopy

Within the canopy, wind shear is created by the air-flow through viscous and bluff-body interactions with phytoelements (Sellers et al., 1996). Aerodynamic resistance below the canopy is a linear function of local wind speed (Denmead, 1976; Legg and Long, 1975). In fact, since the wind speed under the canopy is not too small to be ignored, sensible heat transfer from the ground under the canopy cannot be set to zero even under stable conditions (though some authors assumed). Actually, the wind speed can reach 20% of that above the canopy. The wind-speed profile from the top of the stand to the forest floor can be approximated by merging these two portions together. The upper portion is exponential and lower portion is logarithmic. The merging height is set at $0.2h_c$ (where h_c is the canopy height). The exponential function is

expressed as

$$u_{\text{under,upper}} = u_c \exp\left[-\gamma_a\left(1 - \frac{z}{h_c}\right)\right] \tag{B.1}$$

where $u_{\text{under,upper}}$ is the wind speed at height z within the canopy; γ_a represents the attenuation coefficient; u_c is the wind speed at canopy height. At the height $z = 0.2h_c$, the equation becomes

$$u_{0.2h_c} = u_c \exp[-0.8\gamma_a] \tag{B.2}$$

The value of γ_a is determined by the effective LAI and the structure of the stand. It has been obtained separately for a managed (thinned to 575 stems/ha and pruned to a 6 m height) and unmanaged stand. The experimental results are

$$\gamma_a = \begin{cases} [0.167 + 0.179u_H]L_e^{1/3} & \text{for the managed sand} \\ [0.252 + 0.178u_H]L_e^{1/3} & \text{for the unmanaged sand} \end{cases} \tag{B.3}$$

The logarithmic portion of the profile is expressed as follows:

$$u_{\text{under,lower}} = u_{0.2h_c} \frac{\ln[(z - d_u)/z_{0,M,u}]}{\ln[(0.2h_c - d_u)/z_{0,M,u}]} \tag{B.4}$$

where $u_{\text{under,lower}}$ is the wind speed at height z below $0.2h_c$; $z_{0,M,u}$ is the roughness length of the forest floor for momentum transfer; d_u represents the displacement height at the presence of understorey. At the presence of substantial understorey, $z_{0,M,u} = 0.1h_u$ and $d_u = 0.667h_u$, where the h_u is the average understorey height. In EASS, $z_{0,M,u}$, and d_u are approximately assumed to equal 0.02 and 0 m, respectively. If the mean snow depth is greater than 30 cm, $z_{0,M,u}$ equals 0.005 m.

The aerodynamic resistance for heat and water vapor fluxes under the canopy $r_{a,u}$ is defined

$$r_{a,u} = \frac{1}{(C_{H,u}u_{0.2h_c})} \tag{B.5}$$

where $u0.2_{h_c}$ is the wind speed u at $0.2h_c$; $C_{H,u}$ is the surface drag coefficient for heat fluxes under the canopy. $C_{H,u}$ is calculated using the following equation:

$$C_{H,u} = \left[\frac{k_V}{\ln(0.2h_c - d_u)/z_{0,H,u}}\right]\left[\frac{k_V}{\ln(0.2h_c - d_u)/z_{0,M,u}}\right] \tag{B.6}$$

where k_V is the Von Karman's constant (=0.41). $z_{0,H,u}$ in Eq. (B.6) is the surface roughness length of the forest floor for heat transfer and is estimated following Garratt and Hicks (1973) and Brutsaert (1979):

$$z_{0,H,u} = \frac{z_{0,M,u}}{a_z} \tag{B.7}$$

where a_z is a land cover related parameter varying from 1.5 to 12.0.

B.3. Stomatal resistance

Stomatal resistance at the leaf level r_l (s m^{-1}) is calculated according to Ball et al. (1987):

$$r_l = \left(\frac{\alpha_1 h_s A_l}{C_a + \alpha_2}\right)^{-1} \tag{B.8}$$

where α_1 and α_2 are the parameters representing the composite sensitivity of r_l to leaf surface relative humidity h_s, CO$_2$ concentration C_a (μmol m^{-3}) and leaf net photosynthesis assimilation A_l (μmol m^{-2} s^{-1}).

The bulk stomatal resistance $r_{l,i}$ of the sunlit ($i=1$) and shaded ($i=2$) leaves for water vapor (in s m^{-1}) is calculated using a modified version of the Ball–Woodrow–Berry (Ball et al., 1987) empirical model following Wang and Leuning (1998):

$$\frac{1}{r_{l,i}} = \frac{1}{r_{0,i}} + \frac{mf_w A_{\text{net},i}}{C_{s,i}(1 + D_{s,i}/D_o)}\frac{1}{\bar{\rho}_a} \tag{B.8}$$

where $r_{0,i}$ is the residual resistance (s m^{-1}); $A_{\text{net},i}$ the net photosynthetic rate; $C_{s,i}$ the CO$_2$ mole fraction at the leaf surface (μmol mol^{-1}); $\bar{\rho}_a$ is the mean molar density of dry air; $D_{s,i}$ is the water vapor saturate deficit at the leaf surface (in kPa); D_o is an empirical parameter determining the sensitivity of stomatal conductance to water vapor saturate deficit (in kPa), m is a parameter related to the intercellular CO$_2$ mole fraction by $C_{c,i}/C_{s,i} = 1 - 1/m$ at maximal stomatal opening (when both $D_{s,i}$ and $1/r_{0,i}$ are zero and $f_w = 1$); f_w is a parameter describing the sensitivity of $r_{l,i}$ to soil water availability (Chen et al., 2007).

Following Farquhar et al. (1982), the net carboxylation rate at leaf level is calculated as the minimum of

$$A_{c,i} = V_{c\max}\frac{C_{c,i} - \Gamma_i^*}{C_{c,i} + K_c(1 + O_{c,i}/K_o)} \tag{B.9a}$$

and

$$A_{j,i} = J\frac{C_{c,i} - \Gamma_i^*}{4(C_{c,i} + 2\Gamma_i^*)} \tag{B.9b}$$

where $A_{c,i}$ and $A_{j,i}$ are Rubiso-limited and RuBP-limited gross photosynthesis rates (μmol m^{-2} s^{-1}), respectively. $V_{c\max}$ is the maximum carboxylation rate (μmol m^{-2} s^{-1}); J is the electron transport rate (μmol m^{-2} s^{-1}); $C_{c,i}$ and $O_{c,i}$ are the intercellular CO$_2$ and O$_2$ mole fractions (mol mol^{-1}), respectively; Γ_i^* is the CO$_2$ compensation point without dark respiration (mol mol^{-1}); K_c and K_o are Michaelis–Menten constants for CO$_2$ and O$_2$ (mol mol^{-1}), respectively.

The net photosynthetic rate is calculated as

$$A_{\text{net},i} = \min(A_{c,i}, A_{j,i}) - R_d \tag{B.10}$$

where R_d is the daytime leaf dark respiration and computed as $R_d = 0.015\,V_{c\max}$.

The diffusion of CO$_2$ from the atmosphere into the leaf is also described by

$$A_{\text{net},i} = \frac{(C_{s,i} - C_{c,i})}{(1.6r_{l,i})} = \frac{(C_a - C_{c,i})}{r_{lc,i}} \tag{B.11}$$

where the constant 1.6 is the ratio of the molecular diffusivity of water to that of CO_2; C_a is the ambient CO_2 concentration (μmol mol^{-1}) and $C_{c,i}$ is CO_2 concentration in intercellular of the leaves; $r_{lc,i}$ is the total resistance for CO_2 from the canopy to the intercellular space (s m^{-1}).

Above Eqs. (B.8)–(B.11) and the leaf energy balance equations are solved iteratively for $A_{net,i}$, $r_{l,i}$, $C_{c,i}$, $C_{s,i}$, $D_{s,i}$, and leaf temperatures. The iteration will stop when the difference in temperature between two successive iterations is <0.01 °C for either sunlit or shaded leaves (Wang and Leuning, 1998).

The parameter describing the sensitivity of $r_{l,i}$ to soil water availability f_w in Eq. (B.8) can be integrated from each soil layer's $f_{w,i}$ with a weighting factor w_i:

$$f_w = \sum_{i=1}^{n} f_{w,i} w_i \qquad (B.12)$$

where n is the number of soil layers which contain roots. $f_{w,i}$ is a combined effect of soil water suction (ψ) and temperature ($T_{s,i}$), and it can be described as

$$f_{w,i} = \frac{1}{f_i(\psi_i) f_i(T_{s,i})} \qquad (B.13)$$

where $f_i(\psi)$ and $f_i(T_{s,i})$ are calculated following Zierl (2001) and Bonan (1991), respectively:

$$f_i(\psi_i) = \begin{cases} 1 + (\psi_i/10 - 1)^{\alpha} & \psi_i > 10\,\text{m} \\ 1 & \text{else} \end{cases} \qquad (B.14)$$

$$f_i(T_{s,i}) = \begin{cases} \dfrac{1}{1 - \exp(t_1 T_{s,i}^{t_2})} & T_{s,i} > 0\,°C \\ \infty & \text{else} \end{cases} \qquad (B.15)$$

where α, $T_{s,1}$, and $T_{s,2}$ are empirical parameters and equal to 0.8, −0.04, and 2.0, respectively.

The weighting factor w_i in Eq. (B.9) is calculated as

$$w_i = \frac{r_i f_{w,i}}{\sum_{i=1}^{n} r_i f_{w,i}} \qquad (B.16)$$

where r_i is the root fraction in layer i.

REFERENCES

Anderson, E.A., 1976. A point energy and mass balance model of snow cover, NOAA Tech. Rep. NWS 19, U.S. Dep. of Comm., Silver Spring, MD, 150 pp.

Baldocchi, D.D., Vogel, C.A., Hall, B., 1997a. Seasonal variation of carbon dioxide exchange rates above and below a boreal jack pine forest. Agric. For. Meteorol. 83, 147–170.

Baldocchi, D.D., Vogel, C.A., Hall, B., 1997b. Seasonal variation of energy and water vapor exchange rates above and below a boreal jack pine forest canopy. J. Geophys. Res. (BOREAS Special Issue) 102 (D24), 28939–28952.

Ball, J.T., Woodrow, I.E., Berry, J.A., 1987. A model predicting stomatal conductance and its contribution to the control of photosynthesis under different environmental conditions. In: Biggens, J. (Ed.), Progress in Photosynthesis Research, vol. 4. Martinus-Nijhoff, Dordrecht, Netherlands, pp. 221–224.

Bénié, G.B., Kaboré, S.S., Goïta, K., Courel, M.-F., 2005. Remote sensing-based spatio-temporal modeling to predict biomass in Sahelian grazing ecosystem. Ecol. Model. 184, 341–354.

Bergen, K.M., Dobson, M.C., 1999. Integration of remotely sensed radar imagery in modeling and mapping forest biomass and net primary production. Ecol. Model. 122, 257–274.

Betts, A.K., Ball, J.H., 1997. Albedo over the boreal forest. J. Geophys. Res. 102, 28901–28909.

Black, T.A., den Hartog, G., Neumann, H.H., Blanken, P.D., Yang, P.C., Russell, C., Nesic, Z., Lee, X., Chen, S.G., Staebler, R., Novak, M.D., 1996. Annual cycles of water vapour and carbon dioxide fluxes in and above a boreal aspen forest. Global Change Biol. 2 (3), 219–229.

Blanken, P.D., Black, T.A., Yang, P.C., Neumann, H.H., Nesic, Z., Staebler, R., den Hartog, G., Novak, M.D., Lee, X., 1997. Energy balance and canopy conductance of a boreal aspen forest: partitioning overstory and understory components. J. Geophys. Res. (BOREAS Special Issue) 102 (D24), 28915–28928.

Bonan, G.B., 1991. A biophysical surface-energy budget analysis of soil-temperature in the boreal forests of Interior Alaska. Water Resour. Res. 27, 767–781.

Bonan, G.B., 1995. Land-atmospheric interactions for climate system models: Coupling biophysical, biogeochemical and ecosystem dynamical processes. Remote Sens. Environ. 51, 57–73.

Brutsaert, W.H., 1979. Heat and mass transfer to and from surfaces with dense vegetation or similar permeable roughness. Boundary-Layer Meteorol. 16, 365–388.

Brutsaert, W.H., 1982. Evaporation into the Atmosphere. D. Reidel Publishing Company, Dordrecht, The Netherlands.

Buckingham, E., 1907. Studies on the movement of soil moisture. Bull. 38, USDA Bureau of Soils, Washington, DC.

Campbell, G.S., 1974. A simple method for determining unsaturated conductivity from moisture retention data. Soil Sci. 117, 311–314.

Campbell, G.S., Norman, J.M., 1998. An Introduction to Environmental Biophysics. Springer-Verlag, New York, 285 pp.

Carson, D.J., 1982. Current parameterizations of land-surface processes in atmospheric general circulation models. In: Eagleson, P.S. (Ed.), Land Surface Processes in Atmospheric General Circulation Models. Cambridge University Press, Cambridge.

Chen, J.M., Cihlar, J., 1996. Retrieving leaf area index for boreal conifer forests using landsat TM images. Remote Sens. Environ. 55, 153–162.

Chen, D.-X., Coughenour, M.B., 1994. GEMTM: a general model for energy and mass transfer of land surfaces and its application at the FIFE sites. Agric. For. Meteorol. 68, 145–171.

Chen, J.M., Zhang, R.H., 1989. Studies on the measurements of crop thermal emissivity and sky temperature. Agric. For. Meteorol. 49, 23–34.

Chen, J.M., Yang, B.J., Zhang, R.H., 1989. Soil thermal emissivity as affected by its water content and surface treatment. Soil Science 148, 433–435.

Chen, T.H., Henderson-Sellers, A., Milly, P.C.D., Pitman, A.J., Beljaars, A.C.M., Polcher, J., Abramopoulous, F., Boone, A., Chang, S., Chen, F., Dai, Y., Desborough, C.E., Dickinson, R.E., Dümenil, L., Ek, M., Garratt, J.R., Gedney, N., Gusev, Y.M., Kim, J., Koster, R., Kowalczyk, E.A., Laval, K., Lean, J., Lettenmaier, D., Liang, X., Mahfouf, J.-F., Mengelkamp, H.-T., Mitchell, K., Nasonova, O.N., Noilhan, J., Robock, A., Rosenzweig, C., Schaake, J., Schlosser, C.A., Schulz, J.-P., Shao, Y., Shmakin, A.B., Verseghy, D.L., Wtzel, P., Wood, E.F., Xue, Y., Yang, Z.-L, Zeng, Q., 1997. Cabauw experimental results from the project for Intercomparison of Land-surface Parameterization Schemes. J. Clim. 10, 1194–1215.

Chen, J.M., Liu, J., Cihlar, J., Guolden, M.L., 1999. Daily canopy photosynthesis model through temporal and spatial scaling for remote sensing applications. Ecol. Model. 124, 99–119.

Chen, J.M., Pavlic, G., Brown, L., Cihlar, J., Leblanc, S.G., White, P.H., Hall, R.G., Peddle, D., King, D.J., Trofymow, J.A., Swift, E., Van der Sanden, J., Pellikka, P., 2002. Validation of Canada-wide leaf area index maps using ground measurements and high and moderate resolution satellite imagery. Remote Sens. Environ. 80, 165–184.

Chen, J.M., Liu, J., Leblanc, S.G., Lacaze, R., Roujean, J.-L., 2003. Multi-angular optical remote sensing for assessing vegetation structure and carbon absorption. Remote Sens. Environ. 84, 516–525.

Chen, B., Chen, J.M., Liu, J., Chan, D., Higuchi, K., Shashkov, A., 2004. A vertical diffusion scheme to estimate the atmospheric rectifier effect. J. Geophys. Res. 109, D04306, doi:10.1029/2003JD003925.

Chen, B., Chen, J.M., Worthy, D., 2005a. Interannual variability in the atmospheric CO_2 rectification over a boreal forest region. J. Geophys. Res. 110, D16301, doi:10.1029/2004JD005546.

Chen, J.M., Menges, C.H., Leblanc, S.G., 2005b. Global mapping of foliage clumping index using multi-angular satellite data. Remote Sens. Environ. 97, 447–457.

Chen, B., Chen, J.M., Tans, P.P., Huang, L., 2006a. Modeling dynamics of stable carbon isotopic exchange between a boreal ecosystem and the atmospheres. Global Change Biol. 12, 1842–1867, doi:10.1111/j.1365-2486.2006.01200.x.

Chen, B., Chen, J.M., Huang, L., Tans, P.P., 2006b. Simulating dynamics of $\delta^{13}C$ of CO_2 in the planetary boundary layer over a boreal forest region: covariation between surface fluxes and atmospheric mixing. Tellus (B) 58, 537–549.

Chen, B., Chen, J.M., 2007. Diurnal, seasonal and interannualTemporal variability of carbon isotope discrimination at the canopy level in response to environmental factors in a boreal forest ecosystem. Plant, Cell Environ. 30, doi:10.1111/j.1365-3040.2007.01707.

Chen, B., Chen, J.M., Mo, G., Yuen, C.-W., Margolis, H., Higuchi, K., Chan, D., 2007. Modeling and scaling coupled energy, water, and carbon fluxes based on remote sensing: an application to Canada's landmass. J. Hydrometeorol. 8, 123–143.

Chiesi, M., Maselli, F., Bindi, M., Fibbi, L., Bonora, L., Raschi, A., Tognetti, R., Cermak, J., Nadezhdina, N., 2002. Calibration and application of FOREST-BGC in a Mediterranean area by the use of conventional and remote sensing data. Ecol. Model. 154, 251–262.

Christopher, S.R., Ek, A.R., 2004. A process-based model of forest ecosystems driven by meteorology. Ecol. Model. 179 (3), 317–348.

Cihlar, J., Beaubien, J., Latifovic, R., Simard, G., 1999. Land cover of Canada 1995 Version 1.1. Digital data set documentation, Natural Resources Canada, Ottawa, Ontario. ftp://ftp2.ccrs.nrcan.gc.ca/ftp/ad/EMS/landcover95/.

Clapp, R.B., Hornberger, G.M., 1978. Empirical equations for some soil hydraulic properties. Water Resour. Res. 14, 601–604.

Clark, J.S., Carpenter, S.R., Barber, M., Collins, S., Dobson, A., Foley, J.A., Lodge, D.M., Pascual, M., Pielke, R., Pizer, W., Pringle, C., Reid, W.V., Rose, K.A., Sala, O., Schlesinger, W.H., Wall, D.H., Wear, D., 2001. Ecological forecasts: an emerging imperative. Science 293, 657–660.

Cosby, B.J., Hornberger, G.M., Clapp, R.B., Ginn, T.R., 1984. A statistical exploration of relationships of soil moisture characteristics to the physical properties of soils. Water Resour. Res. 20, 682–690.

Côté, J., Gravel, S., Methot, A., Patoine, A., Roch, M., Staniforth, A., 1998a. The operational CMC-MRB global environmental multiscale (GEM) model. Part I: design considerations and formulation. Monthly Weather Rev. 126, 1373–1395.

Côté, J., Desmarais, J.-G., Gravel, S., Methot, A., Patoine, A., Roch, M., Staniforth, A., 1998b. The operational CMC-MRB global environmental multiscale (GEM) model. Part II: results. Monthly Weather Rev. 126, 1397–1418.

Cox, P.M., Betts, R.A., Bunton, C.B., Essery, R.L.H., Rowntree, P.R., Smith, J., 1999. The impact of new land surface physics on the GCM simulation of climate and climate sensitivity. Clim. Dyn. 15, 183–203.

De Pury, D.G.G., Farquhar, G.D., 1997. Simple scaling of photosynthesis from leaves to canopies without the errors of big-leaf models. Plant Cell Environ. 20, 537–557.

Denmead, O.T., 1976. Teperate cereals. In: Montainth, J.K. (Ed.), Vegetation and the Atmosphere, vol. 2. Academic Press, p. 31.

Dickinson, R.E., Henderson-Sellers, A., Kennedy, P.J., Wilson, M.E., 1986. Biosphere-Atmosphere Transfer Scheme (BATS) for the NCAR Community Climate Model. National Center for Atmospheric Research Tech. Note NCAR/TN-275 + STR, 69.

Dickinson, R.E., Henderson-Sellers, A., Kennedy, P.J., Giorgi, F., 1992. Biosphere–Atmosphere Transfer Scheme (BATS) Version 1.0 as coupled to the NCAR community climate model. Tech Note. National Center for Atmospheric Research, Boulder, CO.

Dickinson, R.E., Shaikh, M., Bryant, R., Graumlich, L., 1998. Interactive canopies for a climate model. J. Clim. 11, 2823–2836.

Eagleson, P.S., 1978. Climate, soil, and vegetation, 3, a simplified model of soil moisture movement in the liquid phase. Water Resour. Res. 14 (5), 722–730.

Entekhabi, D., Eagleson, P.S., 1989. Land surface hydrology parameterization for atmospheric general circulation models including subgrid scale spatial variability. J. Clim. 2, 816–831.

Farquhar, G.D., O'Leary, M.H., Berry, J.A., 1982. On the relationship between carbon isotope discrimination and the intercellular carbon dioxide concentration in leaves. Aust. J. Plant Physiol. 9, 121–137.

Fariouki, O.T., 1981. The thermal properties of snow in cold region. Cold Regions Sci. Technol. 5, 67–75.

Feddes, R.A., Bresler, E., Neuman, S.P., 1974. Field test of a modified numerical model for water uptake by root systems. Water Resour. Res. 10, 1199–1206.

Foley, J.A., Prentice, I.C., Ramankutty, N., Levis, S., Pollard, D., Sitch, S., Haxeltine, A., 1996. An integrated biosphere model of land surface processes, terrestrial carbon balance, and vegetation dynamics. Global Biogeochem. Cycl. 10 (4), 603–628, doi:10.1029/96GB02692.

Friend, A.D., Stevens, A.K., Knox, R.G., Cannell, M.G.R., 1997. A process-based, terrestrial biosphere model of ecosystem dynamics (Hybrid v3.0). Ecol. Model. 95, 249–287.

Garratt, J.R., Hicks, B.B., 1973. Momentum, heat and water vapour transfer to and from natural and artificial surface. Q. J. R. Meterol. Soc. 99, 680–687.

Goetz, S.J., Prince, S.D., Goward, S.N., Thawley, M.M., Small, J., 1999. Satellite remote sensing of primary production: an improved production efficiency modelling approach. Ecol. Model. 122, 239–255.

Graetz, R.D., 1990. Remote sensing of terrestrial ecosystem structure: An ecologist's pragmatic view. In: Hobbs, R.J., Mooney, H.A. (Eds.), Remote Sensing of Biosphere Functioning. Springer–Verlag, New York, pp. 5–30.

Green, W.H., Ampt, G.A., 1911. Studies in soil physics. I. The flow of air and water through soils. J. Agric. Sci. 4, 1–24.

Gustafsson, D., Lewan, E., Lewan, B.J., van den Hurk, J.M., Viterbo, P., Grelle, A., Lindroth, A., Cienciala, E., Mölder, M., Halldin, S., Lundin, L.-C., 2003. Boreal forest surface parameterization in the ECMWF model—1D test with NOPEX long-term data. J. Appl. Meteorol. 42 (1), 95–113.

Henderson-Sellers, Pitman, A.J., Love, P.K., Irannejad, P., Chen, T.H., 1995. The Project for Intercomparison of Land Surface Parameterization Schemes (PILPS): Phases 2 and 3. Bull. Am. Meteorol. Soc. 76, 489–503.

Hillel, D., 1980a. Fundamentals of Soil Physics. Academic Press, New York.

Hillel, D., 1980b. Applications of Soil Physics. Academic Press, New York.

Hutjes, R.W.A., Kabat, P., Running, S.W., Shuttleworth, W.J., Field, C., Bass, B., da Silva Dias, M.F., Avissar, R., Becker, A., Claussen, M., Dolman, A.J., Feddes, R.A., Fosberg, M., Fukushima, Y., Gash, J.H.C., Guenni, L., Hoff, H., Jarvis, P.G., Kayane, I., Krenke, A.N., Liu, C., Meybeck, M., Nobre, C.A., Oyebande, L., Pitman, A., Pielke Sr., R.A., Raupach, M., Saugier, B., Schulze, E.D., Sellers, P.J., Tenhunen, J.D., Valentini, R., Victoria, R.L., Vörösmarty, C.J., 1998. Biospheric aspects of the hydrological cycle. J. Hydrol. 212–213 (1–4), 1–21.

Johansen, O., 1975. Thermal conductivity of soils, Ph.D. thesis, Univ. of Trondheim, Trondheim, Norway.

Jørgensen, S.E., 1994. Fundamentals of Ecological Modelling. Elsevier, Amsterdam.

Kickert, R.N., Tonella, G., Simonov, A., Krupa, S., 1999. Predictive modeling of effects under global change. Environ. Pollut. 100 (1–3), 87–132.

Kite, G.W., Pietroniro, A., 1996. Remote sensing application in hydrological modeling. Hydrol. Sci. 41, 563–591.

Kley, D., Kleinmann, M., Sandermann, H., Krupa, S., 1999. Photochemical oxidants: state of the science. Environ. Pollut. 100 (1–3), 19–42.

Kongoli, C.E., Bland, W.L., 2000. Long-term snow depth simulations using a modified atmosphere-land exchange model. Agric. For. Meteorol. 104, 273–287.

Kucharik, C.J., Foley, J.A., Delire, C., Fisher, V.A., Coe, M.T., Lenters, J.D., Young-Molling, C., Ramankutty, N., Norman, J.M., Gower, S.T., 2000. Testing the performance of a dynamic global ecosystem model: water balance, carbon balance, and vegetation structure. Global Biogeochem. Cycl. 14 (3), 795–826.

Kurth, W., 1994. Morphological models of plant growth: possibilities and ecological relevance. Ecol. Model. 75–76, 299–308.

Lacelle, B., 1998. Canada's soil organic carbon database. In: Lal, R., Kimbla, J., Follett, R.F., Stewart, B.A. (Eds.), Soil Processes and the Carbon Cycle. CRC Press, Boca Raton.

LaChapelle, E.R., 1969. Properties of snow. In: Hydrologic Systems, Coll. of For. Resour., Univ. of Wash., Seattle, p. 21.

Legg, B.J., Long, I.F., 1975. Turbulent diffusion within a wheat canopy. Quart. J. Roy. Meteor. Soc. 101, 611–628.

Letts, M.G., Roulet, N.T., Comer, N.T., Skarupa, M.R., Verseghy, D.L., 2000. Parameterisation of peatland hydrological properties for the Canadian Land Surface Scheme. Atmos. Ocean 38, 141–160.

Liu, J., Chen, J.M., Cihlar, J., Park, W., 1997. A process-based Boreal ecosystems productivity simulator using remote sensing inputs. Remote Sens. Environ. 62, 158–175.

Liu, J., Chen, J.M., Cihlar, J., Chen, W., 1999. Net primary productivity distribution in the BOREAS region from a process model using satellite and surface data. J. Geophys. Res. 104 (D22), 27735–27754.

Liu, J., Chen, J.M., Cihlar, J., Chen, W., 2002. Net primary productivity mapped for Canada at 1-km resolution. Global Ecol. Biogeogr. 11, 115–129.

Liu, J., Chen, J.M., Cihlar, J., Chen, W., 2003. Mapping evapotranspiration based on remote sensing: an application to Canada's landmass. Water Resour. Res. 39 (7), 1189, doi:10.1029/2002WR001680.

Loiselle, S., Bracchini, L., Bonechi, C., Rossi, C., 2001. Modelling energy fluxes in remote wetland ecosystems with the help of remote sensing. Ecol. Model. 145, 243–261.

Maas, S.J., 1988. Use of remotely sensed information in agricultural crop growth models. Ecol. Model. 41, 247–268.

Manabe, S., 1969. Climate and the ocean circulation. 1. The atmospheric circulation and the hydrology of the Earth's surface. Monthly Weather Rev. 97, 739–805.

Masayuki, H., Takayuki, M., 2004. A validation study of a new land surface scheme with the CEOP-1 reference site data set. CEOP Newslett. 6, 3–5.

Mei, R.G., Larson, C.L., 1973. Modeling infiltration during a steady rain. Water Resour. Res. 9, 384–394.

Mellor, M., 1977. Engineering properties of snow. J. Glaciol. 19, 15–66.

Milly, P.C., Eagleson, P.S., 1982. Parameterization of moisture and heat fluxes across the land surface for use in atmospheric general circulation models. Rep. 279, Dept. of Engineering, Massachusetts Institute of Technology, 159 pp.

Monteith, J.L., Unsworth, M.H., 1965. Environmental Physics. Chapman and Hall Inc, pp. 227 (Chapter 13).

Monteith, J.L., Unsworth, M.H., 1990. Principles of Environmental Physics, second ed. Chapman and Hall Inc., Arnold, London.

Norman, J.M., 1980. Interfacing leaf and canopy light interception models. In: Hesketh, J.D., Jones, J.W. (Eds.), Predicting Photosynthesis for Ecosystem Models. CRC, Boca Raton, pp. 49–68.

Norman, J.M., 1982. Simulation of microclimates. In: Hatfield, J.L., Thomason, I.J. (Eds.), Biometeorology in Integrated Pest Management. Academic Press, New York, pp. 65–99.

Ogee, J., Brunet, Y., 2002. A forest floor model for heat and moisture including a litter layer. J. Hydrol. 255, 212–233.

Patankar, S.V., 1980. Numerical Heat Transfer and Fluid Flow. McGraw-Hill, New York, p. 197.

Peart, R.M., Curry, R.B., 1998. Agricultural Systems Modeling and Simulation. Marcel Dekker, Inc., New York.

Philip, J.R., 1957. The theory of infiltration. 1. The infiltration equation and its solution. Soil Sci. 83, 345–357.

Pitman, A.J., Yang, Z.-L., Cogley, J.G., Henderson-Sellers, A., 1991. Description of bare essentials of surface transfer for the Bureau of Meteorology Research Center AGCM. BMRC Research Report No. 32, Melbourne, Victoria.

Pleim, J.E., Xiu, A., 2003. Development of a land surface model. Part II. Data assimilation. J. Appl. Meteorol. 42, 1811–1822.

Plummer, S.E., 2000. Perspectives on combining ecological process models and remotely sensed data. Ecol. Model. 129, 169–186.

Radcliffe, D.E., Rasmunssen, T.C., 2000. Soil water movement. In: Sumner, M.E. (Ed.), Handbook of Soil Science. CRC Press, New York, pp. A87–A127 (Chapter 4).

Rango, A., Shalaby, A.I., 1999. Urgent Operational Applications of Remote Sensing in Hydrology, World Meteorological Organization, Operational Hydrology Report No. 43, Secretariat of World Meteorological Organization, Geneva, Switzerland.

Rawls, W.J., Ahuja, L.R., Brakensiek, D.L., 1992. Estimating soil hydraulic properties from soils data. In: Van Genuchthen, M.th., Leij, F.J., Lund, L.J. (Eds.), Indirect Methods for Estimating Hydraulic Properties of Unsaturated Soils. U.C. Riverside Press, Riverside, CA.

Richards, L.A., 1931. Capillary conduction of liquids in porous mediums. Physics 1, 318–333.

Running, S.W., Coughlan, J.C., 1988. A general model of forest ecosystem processes for regional applications. I. Hydrologic balance, canopy gas exchange and primary production processes. Ecol. Model. 42, 125–154.

Saunders, I.R., Bowers, J.D., Huo, Z., Bailey, W.G., Verseghy, D., 1999. Simulation of alpine tundra surface microclimates using the Canadian Land Surface Scheme. I. Albedo and net radiation modelling. Int. J. Climatol. 19 (8), 913–926.

Schut, P., Shields, J., Tarnocai, C., Coote, D., Marshall, I., 1994. Soil Landscapes of Canada—An Environmental Reporting Tool Canadian Conference on GIS Proceedings, June 6–10, 1994, Ottawa, pp. 953–965.

Schwalm, C.R., Ek, A.R., 2001. Climate change and site: relevant mechanisms and modeling techniques. For. Ecol. Manage. 150 (3), 241–258.

Seaquist, J.W., Olsson, L., Ardö, J., 2003. A remote sensing-based primary production model for grassland biomes. Ecol. Model. 169, 131–155.

Sellers, P.J., Mintz, Y., Sud, Y.C., Dalcher, A., 1986. A simple biosphere model (SiB) for use within general circulation models. J. Atmos. Sci. 43, 505–531.

Sellers, P.J., Randall, D.A., Collatz, G.J., Berry, J.A., Field, C.B., Dazlich, D.A., Zhang, C., Collelo, G.D., Bounoua, L., 1996. A revised land surface parameterization (SiB2) for atmospheric GCMs. Part I. Model formulation. J. Clim. 9, 676–705.

Sellers, P.J., et al., 1997. Modeling the exchange of energy, water, and carbon between continentals and the atmosphere. Science 275, 502–509.

Shields, J.A., Tarnocai, C., Valentine, K.W.G., MacDonald, K.B., 1991. Soil landscapes of Canada, Procedures manual and user's hand book. Agriculture Canada, Agriculture Canada Publication 1868/E, Ottawa, Ontario.

Stieglitz, M., Rind, D., Famiglietti, J., Rosenzweig, C., 1997. An efficient approach to modeling the topographic control of surface hydrology for regional and global climate modeling. J. Clim. 10, 118–137.

Sun, S.F., 1982. Moisture and heat transport in a soil layer forced by atmospheric conditions, M.S. Thesis, Univ. of Conn., Storrs.

Tarnocai, C., 1996. The amount of organic carbon in various soil orders and ecological provinces in Canada. In: Lal, R., Kimbla, J., Follett, R.F., Stewart, B.A. (Eds.), Soil Processes and the Carbon Cycle. CRC Press, Boca Raton, FL, pp. 81–92.

Thom, A.S., Oliver, H.R., 1997. On Penman's equation for estimating regional evaporation. Q. J. R. Meteorol. Soc 103, 345–357.

Tjernatrom, M., 1989. Some tests with a surface energy balance scheme, including a bulk parameterization for vegetation, in mesoscale model. Boundary-Layer Meteorol. 48, 33–68.

Toconet, O., Bernard, R., Vidal-Madjar, D., 1986. Evapotranspiration over an agricultural region using a surface flux/temperature model based on NOAA-AVHRR data. J. Clim. Appl. Meteorol. 25, 284–307.

Verseghy, D.L., 1991. CLASS: a Canadian land surface scheme for GCMs. I. Soil model. Int. J. Clim. 11, 111–133.

Verseghy, D.L., McFarlane, N.A., Lazare, M., 1993. CLASS: a Canadian land surface scheme for GCMs. II. Vegetation model and coupled runs. Int. J. Clim. 13, 347–370.

Viterbo, P., Beljaars, A.C.M., 1995. An improved land surface parameterization scheme in the ECMWF model and its validation. J. Clim. 8, 2716–2748.

Wang, S., Grant, R.F., verseghy, D.L., Black, T.A., 2002a. Modeling carbon-coupled energy and water dynamics of boreal aspen forest in a general circulation model land surface scheme. Int. J. Clim. 22, 1249–1265.

Wang, S., Grant, R.F., verseghy, D.L., Black, T.A., 2002b. Modeling carbon dynamics of boreal forest ecosystems using the Canadian land surface scheme. Clim. Change 55, 451–477.

Wang, Y.P., Leuning, R., 1998. A two-leaf model for canopy conductance, photosynthesis and partitioning of available energy I: Model description and comparison with a multi-layered model. Agric. Forest Meteorol. 91, 89–111.

Williams, P.J., Smith, M.W., 1989. The Frozen Earth: Fundamentals of Geocryology. Cambridge University Press, New York, 306 pp.

Williams, M.S., Law, B.E., Anthoni, P.M., Unsworth, W.H., 2001. Use of a simulation model and ecosystems flux data to examine carbon-water interactions in ponderosa pine. Tree Physiol. 21 (5), 287–298.

Zhang, Y., Chen, W., Cihlar, J., 2003. A process-based model for quantifying the impact of climate change on permafrost thermal regimes. J. Geophys. Res. 108 (D22), 4695, doi:10.1029/2002JD003354.

Zierl, B., 2001. A water balance model to simulate drought in forested ecosystems and its application to the entire forested area in Switzerland. J. Hydrol. 242, 115–136.